University of Kent

Kent Academic Repository

Burchell, M.J., Alesbrook, L.A., van Ginneken, M. and Wozniakiewicz, P.J. (2026) ***Hypervelocity perforation of thin films applicable to debris detection in low earth orbit*****. Acta Astronautica, 243 . pp. 73-90. ISSN 0094-5765.**

Downloaded from

https://kar.kent.ac.uk/112848/ The University of Kent's Academic Repository KAR

The version of record is available from

https://doi.org/10.1016/j.actaastro.2026.01.050

This document version

Publisher pdf

DOI for this version

Licence for this version

CC BY (Attribution)

Additional information

Versions of research works

Versions of Record

If this version is the version of record, it is the same as the published version available on the publisher's web site. Cite as the published version.

Author Accepted Manuscripts

If this document is identified as the Author Accepted Manuscript it is the version after peer review but before type setting, copy editing or publisher branding. Cite as Surname, Initial. (Year) 'Title of article'. To be published in ***Title of Journal*** , Volume and issue numbers [peer-reviewed accepted version]. Available at: DOI or URL (Accessed: date).

Enquiries

If you have questions about this document contact ResearchSupport@kent.ac.uk. Please include the URL of the record in KAR. If you believe that your, or a third party's rights have been compromised through this document please see our Take Down policy (available from https://www.kent.ac.uk/guides/kar-the-kent-academic-repository#policies).

Acta Astronautica 243 (2026) 73–90

Contents lists available at ScienceDirect

Acta Astronautica

journal homepage: www.elsevier.com/locate/actaastro

Hypervelocity perforation of thin films applicable to debris detection in Low Earth Orbit

M.J. Burchell, L.A. Alesbrook, M. van Ginneken, P.J. Wozniakiewicz *

Centre for Astrophysics and Planetary Science, School of Engineering, Mathematics and Physics, University of Kent, Canterbury, Kent, CT2 7NH, United Kingdom

ARTICLE INFO

Keywords:
Hypervelocity
Penetration
Thin films
Orbital debris
Cosmic dust

ABSTRACT

The growth in the number of satellites in Low Earth Orbit, coupled with the possibility of their catastrophic disruption, may lead to more orbital debris, which in turn has increased the risk of damage to spacecraft arising from impacts by small pieces of debris. There is thus an urgent need to monitor the small particle population in Low Earth Orbit, using a new generation of dust detectors. Various designs are in preparation, and several use the principle of observing particles via their impact penetration of thin films. Previously, most laboratory studies of penetration of thin films have used spherical impactors for ease. However, these are not representative of the shapes of orbital debris. Accordingly, here, impacts are reported at 5 km s^{-1}, by various shaped projectiles (sizes typically 0.5–2 mm) on thin (12.5 μm thick) Kapton films. The shapes used were spheres, rods, cubes and platelets, and represent a selection of the shapes present in the orbital debris population that arises from catastrophic disruption of spacecraft. The size and shape of the holes in the Kapton arising from the impacts, are shown to reflect the size and cross-sectional area of an impactor as it passes through the film; even the presence of angular corners in the impactors can be seen in the holes. However, due to the variable aspect of an individual impactor presented to the film during an impact, identification of the exact 3-dimensional shape cannot be obtained from the 2-dimensional hole. Nevertheless, with minor exceptions it is possible to separate more spherical (i.e., natural dust) impactors from the other shapes (i.e. variously shaped anthropogenic debris).

1. Introduction: Debris in Low Earth Orbit

Anthropogenic debris in Earth orbit poses an increasing hazard to satellites and other spacecraft (e.g., see Refs. [1–3]). The debris has a variety of origins and sizes. At small sizes (μm to 10s of μm scale) it can be material that is emitted in propellant (e.g., aluminium oxide additives to propellant to ensure even burn). At scales of 100s of μm to mm and even cm, material may be released as ejecta or spall fragments after impact by a natural cosmic dust particle or another piece of debris, or may degrade from the surface of a satellite due to environmental effects. At larger, metre-scales, dead satellites or even entire rocket upper stages (that remain in space after their use and which are no longer under control), can be considered as a hazard and are thus also classed as debris. The accidental disruption of a satellite due to an internal explosive event (an explosive event in a battery, sudden ignition of stored propellant, etc.), or even deliberate destruction via an anti-satellite interceptor, can also release showers of debris (e.g., see Ref. [4]). Disruption of a satellite can also arise from collision with a large enough piece of debris or another satellite.

The risk is that, once released, debris of any size may impact another space vehicle. Such impacts have long been recognised as a hazard for spacecraft (e.g., see Ref. [5]). The impacts can, depending on impactor size, produce a crater in a relatively thick target, penetrate thin plates (causing damage in the interior of the vehicle), or even catastrophically disrupt the whole spacecraft resulting in a large number of fragments of varying size, shape and composition (see Ref. [6], for an early discussion of this issue). Impact cratering and penetration can generate some additional debris fragments, with a small multiplier effect. However, if a catastrophic impact occurs, it will generate large quantities of debris and there may be a sufficient multiplier effect to enable a subsequent impact by some of this debris on another spacecraft, yielding yet more debris, leading to a further impact and so on. This runaway cascade-like effect is the so-called Kessler syndrome (e.g., see Refs. [1,6–8]).

According to the European Space Agency (ESA), there were over 12,000 payloads in Earth Orbit in 2024 and over 36,000 trackable objects [3]. To put this into perspective, the same report suggests that a decade earlier there were only some 3500 payloads and 12,000 trackable objects. Given the rapidly increasing number of objects in Earth orbit, the debris problem is likely growing worse.

* Corresponding author.
E-mail address: p.j.wozniakiewicz@kent.ac.uk (P.J. Wozniakiewicz).

https://doi.org/10.1016/j.actaastro.2026.01.050
Received 19 December 2025; Received in revised form 20 January 2026; Accepted 21 January 2026
Available online 22 January 2026
0094-5765/© 2026 The Authors. Published by Elsevier Ltd on behalf of IAA. This is an open access article under the CC BY license (http://creativecommons.org/licenses/by/4.0/).

List of abbreviations:

CFRP	Carbon fibre reinforced plastic
ESA	European Space Agency
HVI	Hypervelocity impact
LEO	Low Earth Orbit
MLI	Multi-layer insulation
NaCl	Sodium chloride salt
Q	Impact energy density
Q^*	Critical value of impact energy density which just causes catastrophic disruption (i.e., where the largest surviving fragment has a mass 50 % of that of the initial target body)
SDS	Space Debris System (NASA instrument to measure dust in space)
SOCIT	Satellite Orbital Debris Characterization Impact Test
STS	Space Transportation System (NASA space shuttle)

It is not yet clear if the amount of debris in orbit combined with the increasing number of satellites, has yet made the Kessler syndrome inevitable. Nevertheless, to reduce this risk, several space agencies have adopted mitigation strategies that include improved design to reduce release of surface material due to degradation in the space environment, more rapid de-orbiting of spacecraft at their end of life, new missions to actively de-orbit dead objects in orbit, mandatory collisional avoidance manoeuvre capability, and so on (e.g., see Ref. [9], or [10]). There have also been many studies of impact damage in the hypervelocity regime aimed at better understanding the mechanisms of impact damage (and the associated release of ejecta) and catastrophic disruption of constructed objects such as spacecraft in hypervelocity impact events.

In the rest of the Introduction, typical impact speeds and their consequences are given. Then debris shapes, composition, size, and flux in Low Earth Orbit (LEO) are all discussed. This is followed by a discussion of the need for more data on the response of thin films to highspeed impacts by different shaped projectiles, which is the focus of the experimental programme reported in the rest of the paper. Thin films are important, as a new generation of impact detectors, which will monitor the debris flux in LEO, rely on use of thin films as the active target area.

1.1. Impact speeds

Software packages such as NASA's ORDEM [11] and ESA's MASTER [12], provide details of the potential impactor flux and impact speed likely to be encountered in a given orbit. Analytic estimates of the impact speed are also possible, and a convenient parametrization of the debris impact speed is provided by Ref. [13]. For LEO, this parametrization (see eqn. (5) in Ref. [13]) averages over altitude but has an explicit dependence on the inclination i of the orbit of the target body. The result is shown in Fig. 1, where the distribution of debris impact speeds is given for three values of target body orbit inclination which cover a range of typical applications. The low inclination ($i = 30°$) provides coverage of equatorial regions, the mid inclination includes several thousand Starlink satellites at $i = 53°$ (as well as the International Space Station at $i = 51.6°$), and the high inclination represents near polar orbits which permit global coverage (including, for example, over 200 Starlink satellites, to date, at $i = 97.6°$, with several thousand more planned).

The resulting debris impact speeds in Fig. 1, vary noticeably with inclination. The higher inclinations provide the highest speeds (a relatively narrow distribution between 13 and 15.5 km s^{-1}, with modal impact speed around 15 km s^{-1}). Then, as the inclination lowers, the modal impact speed falls to around 13.5 km s^{-1} at $i = 53°$ and 13 km s^{-1} at $i = 30°$. At these lower inclinations, there is also a broad shoulder at lower speeds (some 7–11 km s^{-1}), whose relative intensity increases as the inclination reduces.

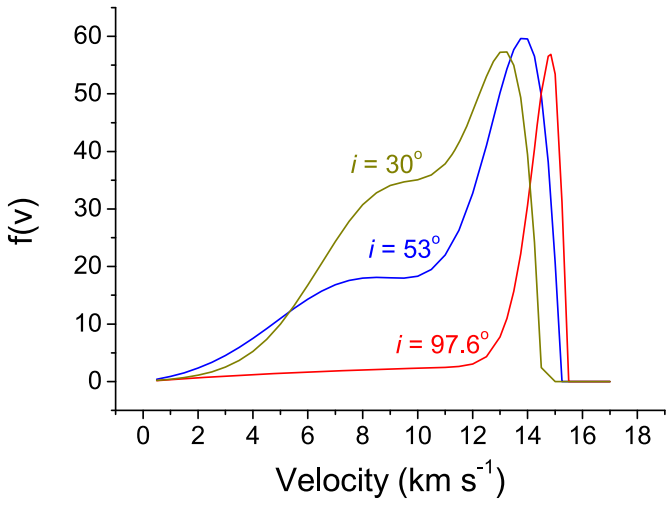


Fig. 1. Impact speed of debris on a satellite in Low Earth Orbit. Three orbital inclinations are shown, with $i = 30°$ covering equatorial latitudes, $i = 53°$ being that of several thousand Starlink satellites, and $i = 97.6°$ being typical of near polar orbiting satellites (e.g., several hundred Starlink satellites to date with more planned).

1.2. Hypervelocity impact

As can be seen from Fig. 1, the debris impact speed in LEO is some 2–15 km s^{-1}, depending on the inclination of the orbit. This compares to a mode impact speed of some 15–20 km s^{-1} for impacts by natural, cosmic dust (this can vary depending on the dust's heliocentric orbit - if prograde the speed can fall to some 7–8 km s^{-1}, or rise to a maximum of 72 km s^{-1} for a retrograde orbit). The significance of this is that all these speeds fall into the regime commonly referred to as hypervelocity. During a hypervelocity impact (HVI), the resulting shock waves in both target and impactor, exceed the local sound speed, resulting in high shock pressures and shattering, melting and even vaporisation of parts of the impactor and target. The transition to the HVI regime is typically for impact speeds above 1–3 km s^{-1}, and HVI has long been recognised as a hazard for spacecraft (e.g., see Ref. [5]).

1.3. Target response to hypervelocity impact (including catastrophic disruption)

There is an extensive literature on material response under HVI, where the key regimes are cratering, penetration, and catastrophic disruption. These outcomes depend not only on impact speed, but also on composition (of both impactor and target) and variables such as the ratio of target thickness (t) to projectile diameter (d), where low t/d values can lead to penetration, e.g. see Ref. [14] for details of penetrations in metal (aluminium) and Teflon plates, see Ref. [15] for penetration of thin films, or see Ref. [16] for modelling of penetration of carbon fibre reinforced plastic (CFRP) plates. The ductile or brittle nature of the target is also important, with the former producing bowl-shaped craters and the later, wider spallation dominated craters, releasing more slow moving, large spall fragments (e.g., see Refs. [5,17,18]).

A key parameter in a HVI event is often taken as the overall energy density Q, defined as the kinetic energy of the impactor divided by the target mass. Strictly speaking, the divisor in Q should be the sum of both target and impactor masses, but since the former is usually significantly greater than the latter, the impactor mass is commonly neglected. At low Q values, cratering occurs. Then, as Q increases, the Q value at which the

largest surviving fragment has ½ the mass of the original pre-impact target, is defined as Q^* and taken as representing the onset of catastrophic disruption. Above this value of Q, the mass of the largest fragment falls rapidly, and the number of fragments increases significantly.

Most studies of catastrophic disruption assume the target body is a solid, homogeneous sphere. This permits ready study in the laboratory or via modelling, and extrapolation of results to different size scales. It should be noted that Q^* itself falls as target size increases, by a factor of about 4 for each order of magnitude increase in size (e.g., see Fig. 7 in Ref. [19]) as a result of effective strength weakening of larger bodies. At still larger sizes of the pre-impact target body, typically of order 100–1000 m, the self-gravity of the resulting fragments means they can start to coalesce after the impact, leaving a post-impact body which is larger than that of any individual fragment. At this size scale and above, the effective Q^* needed to produce a largest final, post-impact body of ½ the original mass, thus starts to increase as extra energy is now needed to not just fragment the original target, but also disperse the fragments against the self-gravitation effect. This contribution to Q^* now exceeds that needed to disrupt the body, and dominates the combined Q^* value at these larger sizes. Given the mass of typical satellites, they fall well within the strength dominated regime, and this self-gravitating effect can be ignored.

However, for a spacecraft one cannot simply use the Q^* value for an equal mass of metal, or glass, or plastic etc. This is because spacecraft are of a non-homogeneous composition (i.e., contain many different materials, such as different metals, glass, carbon-fibre based material, wiring, circuit boards, etc.) and also contain significant macroporosity, both of which influence the value of Q^*. This makes the determination of Q^* for a spacecraft difficult. For many years, NASA's Standard Satellite Breakup Model has used a figure of 40 kJ kg^{-1} as the appropriate value of Q^* for a spacecraft (e.g., Ref. [20]). This can be contrasted with Q^* for solid, homogeneous targets. A summary of early laboratory measurements for various target types of size of order 1–10 cm, reported Q^* was typically in the range of ten to a few thousand J kg^{-1} [21]. In general, Q^* is of order 1000 J kg^{-1} for solid glass spheres [22], in the range 500–2000 J kg^{-1} for 10 cm width rocky objects (see Ref. [23] for a discussion), and 8700–13,000 J kg^{-1} for 4 cm width iron targets [24], i.e., all notably lower than the NASA value for an inhomogeneous, distributed body such as a satellite.

As stated, as well as composition, the influence on Q^* of macroporosity is important. For example, the influence of large internal voids on Q^* can be seen from the change in Q^* for solid ice (18 J kg^{-1}) vs. hollow ice (25 J kg^{-1}) targets [25,26], where a significant macroporosity of 60 % increased the Q^* value by 50 %. In this case, the increase in Q^* was observed to arise from the need for a similar impact energy in both cases (as distinct from energy density), with the reduction in target mass causing the increase in the Q^* value.

In addition, some satellites rotate, and the effect of target rotation has also been considered in laboratory experiments. For 6–8 cm diameter cement targets, Q^* falls by 1/3, from 1447 ± 90 J kg^{-1} (static) to 987 ± 349 J kg^{-1} (rotating at 3.4 Hz) [23]. This effect is held to be due to centrifugal effects causing crack propagation to be enhanced. In principle, Q^* could also be reduced if an impact occurs and triggers the detonation of an energetic source inside a spacecraft (such as a propellant tank or battery). Depending how much energy is stored in such a device, it could contribute to the breakup of the spacecraft.

What a single value of Q^* for spacecraft does not allow for, however, is where the impact occurs on a spacecraft. For example, if struck on a solar panel, a large enough impactor can penetrate and the resulting debris cloud then continues into free space beyond the panel, and not into the interior of the spacecraft as it would if the impact were on the spacecraft main bus. Some of the impact shock is retained by the solar panel, which could fragment and break apart, or separate from the main spacecraft. But detailed studies are needed to determine the energy densities needed for this.

An extreme case of impacts on relatively thin flat surfaces, is an impact on a thin film (thickness of a few tens of μm) such as Kapton. Even relatively small particles will penetrate (see the discussion in section 4.2), transferring only a fraction of their energy/momentum to the thin film. The degree of disruption of the impactor as it penetrates may be minimal, so it can subsequently penetrate a second film in similar fashion (use of this is made in two layer dust impact detectors, which use the time of flight between the layers to determine particle speed, e.g., Ref. [27], or, for a recent discussion see Ref. [28]). If the rear of a structure of several thin Kapton layers is open to space (as distinct from being solid, or leading into the interior of the spacecraft), it is not clear what a catastrophic energy limit means in such cases.

A further complication is if a large area thin film (or solar sail) is used in a mission, and is deployed on booms (such as proposed in Ref. [29]). The film may have a large area (10s of m^2), with a subsequent high probability over time of being impacted by a large piece of dust/debris, but the damage will be minimal. The booms will, however, be only lightly shielded at best, so will be vulnerable, with a low Q^* value typical of normal density materials as indicated above. The main spacecraft bus will likely be shielded as usual, and there the Q^* value of 40 kJ kg^{-1} will apply. Any mission constraints on the total flux of larger (mm or cm) sized impactors (required by space agencies for example) will then apply to the booms and spacecraft main bus, but not the thin film/sail which will comprise the largest exposed surface area of the whole spacecraft. A detailed analysis of the risk of impact damage to such bodies will thus be required, with different standards applied to the main components (large area thin film or solar sail, vs. booms and the main spacecraft body).

1.4. Laboratory tests of satellite catastrophic disruption

It is thus no surprise that it has long been held that the complex design of spacecraft could significantly influence the outcome of a catastrophic disruption event (e.g., Ref. [6]). Accordingly, in 1992 NASA conducted a laboratory impact experiment called SOCIT(4), using an US Navy Transit satellite as the target. This satellite (see Table 1 for key details) was considered representative of typical spacecraft at the time. The number of fragments vs. mean size was obtained and used in the NASA Standard Breakup Model, and has subsequently been compared at large fragment sizes to what was observed in on-orbit breakups of satellites (e.g. Ref. [4]), or with the results of impact modelling (e.g., Ref. [30]).

Since the SOCIT(4) test, a variety of other such laboratory tests have also been carried out on representative satellite bodies (again see Table 1), the best known of which is DebriSat [31,36,37]. Beyond just reporting fragment numbers, some experiments also gave details on both fragment composition and shape vs. size (see Table 2). In parallel, models often break debris composition down into three classes – low density (1200 kg m^{-3}, e.g., plastics), medium density (2500 kg m^{-3}, e.g., aluminium, glass) and high density (7800 kg m^{-3}, e.g., copper, steel), with mid-density taken as the most frequent.

Whilst it can be difficult to compare all the experiments in Tables 1 and 2, some general observations can be made. Firstly, the Q^* value of 40 kJ kg^{-1} appears broadly correct. Next, the use of experiments at impact speeds below a few km s^{-1} is not problem free, and there are some subtle effects on fragmentation as the impact speed increases from 1, to say 3 or 4 km s^{-1} (i.e., in the transition to the hypervelocity regime). Then, when considering the presence or absence of some materials in the ejecta, the presence of such materials in the original target needs to be checked. Not all experiments had the same target composition, and some materials, such as CFRP (which has become prevalent in spacecraft construction in recent years), were not used in SOCIT(4) for example. Finally, the detailed shape of the fragments has become a focus of further study in recent years. The initial 10 classes of shape reported from SOCIT(4) were reduced to 6 main classes in the DebriSat results (see Table 2, or [36,31]). However, not all shapes are equally frequent at

Table 1
Key details of various laboratory experiments wherein a satellite or satellite mock-up was impacted in the laboratory and catastrophically disrupted by impacts at > 1 km s^{-1}. In each case (except the CNES/JANUS picosat), target fragmentation occurred.

Test Name	Date	Target mass (kg)	Target size (m)	Impact speed (km s^{-1})	Impactor mass (kg)	Impact energy density Q (kJ kg^{-1})	Debris Shape reported?	Reference
SOCIT(4)	1992	34.5	0.46 (w) × 0.30 (h)	6.1	0.15	81	Y	[31,32]
CANSAT Microsatellite (cylindrical shape)	2005	0.680	0.14 (w) × 0.16 (h)	1.35	0.036	48	N	[33]
Microsatellite 2005 (cube shape, 2 tests)	2005	0.74	0.15 × 0.15 × 0.15	(a) 1.45 (b) 4.44	(a) 0.040 (b) 0.004	55	Y	[34]
Microsatellite 2007 (3 tests)	2007	1.28–1.30	0.20 × 0.20 × 0.20	1.66, 1.66, 1.72	0.039	41.5 42.0 45.1	Y	[35]
DebriSat	2016	56	0.60 (w) × 0.50 (h)	6.8	0.570	235	Y	[31,36, 37]
DebrisLV	2016	17.1	0.35 (w) × 0.88 (h)	6.9	0.598	832	Y	[31,36, 37]
CARDC Microsatellite (3 tests)		7.295, 8.183 13.10,	0.40 × 0.40 × 0.40	3.26, 3.04, 3.61	0.097	71.12, 54.86, 48.21	Y, 4 shapes	[38]
CNES/JANUS Picosat	2021	0.845	0.15 × 0.10 × 0.10	6.690	0.00072	19.0[a]	N	[39]
Picosat	2022	0.07629	0.05 × 0.05 × 0.05	2.72	0.0016	80.65		[40]

[a] This impact energy density is less than the 40 kJ kg^{-1} suggested by NASA, and did not destroy the target.

Table 2
Characteristic debris shapes reported by disruption of satellites in laboratory testing. Note: carbon fibre reinforced plastic was not a major component in the targets in the SOCIT(4) or CARDC tests.

Test name	Number of classes of fragment shape	Name and key characteristics of each fragment shape	Fragment Composition	Comment	Reference
SOCIT(4)	10	Flat plates Curved plate Box Sphere Flake Rod Cylinder Box and plate Nugget Other	Aluminium Steel Copper Phenolic/plastic Fibreglass Other	Composition: Metals were dominated by Al (96 %). Non-metallics and other were dominated by phenolic/plastic (88 %). Shape: Nuggets dominate below 2 mm (in the ratio 4:1 plastic:metal).	[32]
Microsatellite (2005)	2	Plate-like Needles	Distinct low and high density fragments	Fragment sets similar in magnitude, but relatively more 1+cm sized fragments at higher speed, which contained many carbon fibre reinforced plastic fragments. No detailed shape given, except the higher speed impact had more line-shape fragments than at lower speed.	[34]
Microsatellite (2007)	2	Plate-like Needles	Distinct low and high density fragments (carbon fibre reinforced plastic and metal dominated respectively)	Lenth to width ratio ranges from 1 to 100 with two peaks (at 1 and 10); width to depth ratio ranges from 1 to 100 (with a peak at 10).	[35]
DebriSat and DebrisLV	6	Straight rod Flat plate Flexible Bent rod Nugget Bent plate	Carbon fibre reinforced plastic Plastic Epoxy Copper Other metals, i.e. Ti, Al, St. st. Glass	Composition: Metal dominates above 15 mm, carbon fibre reinforced plastic below 15 mm. Shape: Nuggets dominate above 19 mm. Below 19 mm, platelets dominate.	[31]
CARDC Microsatellite	4	Plate Hexagon Warped/irregular Line shape	Aluminium Circuit board Steel bolts Electronic components	Numerically, aluminium dominated the collected fragments (72–91 %), then circuit board (7–25 %), with steel (0.5–1.3 %). Different shapes were dominated by different density materials.	[38]

all sizes, due to the way target bodies fragment, and this also needs to be taken into account when considering impact outcomes.

The latter points are increasingly considered important. It has long been known that projectile composition (e.g., density and strength) can influence the outcome of an impact (e.g. depth, diameter, volume of a crater, etc.), and so can projectile shape. For example, it was shown over 50 years ago that long cylinders were more effective at penetrating metal plates than spheres of equal mass [41]. Regarding cratering, there have long been various studies of effects of non-spherical impactors. For example, normal incidence impacts on metal targets by spheres (cellulose acetate, aluminium and stainless steel), are compared with those by rods (copper) and hexagonal platelets (plastic) in Ref. [42]. Later, Ref. [43] compared craters made during impacts in space by real mineral grains with those in the laboratory from a variety of mineral impactors (including needle shaped grains of Wollastonite, density 2800 kg m^{-3}, which, depending on the aspect at impact, could produce long, narrow craters, also see Fig. 1 in Ref. [44]). Recently, with the renewed interest after DebriSat, the issue of impactor shape and composition has again become of great interest in penetration of spacecraft shielding and catastrophic disruption (e.g., see Ref. [45] for a review). For example, Ref. [46] reports on HVI tests of shielding in the laboratory, using disk shaped impactors of CFRP, steel and copper, with length to width ratios

for CFRP of 1:3 and 1:5, for steel of 1:3, 2:3, 3:1, and for copper of 2:3 and 3:1, showing that, at equal mass, these tend to be more damaging that spherical impactors. Similarly, Ref. [47] has reported on the relative penetration properties of spheres, rods, nuggets and disks impacting bumpershields. However, there is limited discussion of the effects of such impacts on thin films.

1.5. Impactor size associated with the onset of catastrophic disruption

If 40 kJ kg^{-1} is taken as the appropriate value of Q^* for a satellite, then the size of an impactor necessary to just cause catastrophic disruption for a given mass spacecraft can be readily calculated. The key variables in such a calculation are the target mass, and impactor speed and density. Assuming spherical projectiles, the critical impactor diameter (at typical densities) to just cause catastrophic disruption at three different target body masses is shown vs. impact speed in Fig. 2, and briefly summarised at indicative speeds of 5, 10 and 15 km s^{-1} in Table 3. In this analysis, a target mass of 800 kg was selected as being that of the rapidly increasing population in LEO of Starlink V2 satellites, 100 kg was taken as typical of a small satellite bus with no solar panels (e.g., that of the OneWeb satellites without their solar panels), and 6 kg as that for a 3U cubesat (several thousand cubesats have been launched into orbit to date [48], with about 2/3 in the 3U category [49]). The impactor diameter necessary to cause catastrophic disruption ranges from some 8–160 mm (Table 3). It should thus be no surprise, that, in general, even mm sizes can cause significant damage to a spacecraft which, whilst short of catastrophic, can damage critical components or stop a spacecraft functioning (e.g., see Table 1 in Ref. [50] for a description of typical types of damage vs. impactor size).

1.6. Measuring the mm – cm flux in Low Earth Orbit

Knowledge of the flux of mm – cm sized objects in LEO is thus clearly vital, and, for example, most agencies require satellite operators to model the expected impact flux on their satellite in advance of launch, with a view to minimising the risk of operational loss or catastrophic disruption. The modelling tools commonly used, such as MASTER and ORDEM, incorporate previously measured flux rates (and extrapolations thereof), and then generate the impact flux for the required spacecraft in its specified orbit in a given epoch. However, the sources of the input flux are not necessarily well constrained. They rely on ground radar measurements of objects in orbit (typically of order 10 cm or larger in size to provide tracking data, with smaller cm size objects detectable but not trackable), and, for smaller objects, use historical measurements made in orbit by various detectors or from analysis of retrieved surfaces.

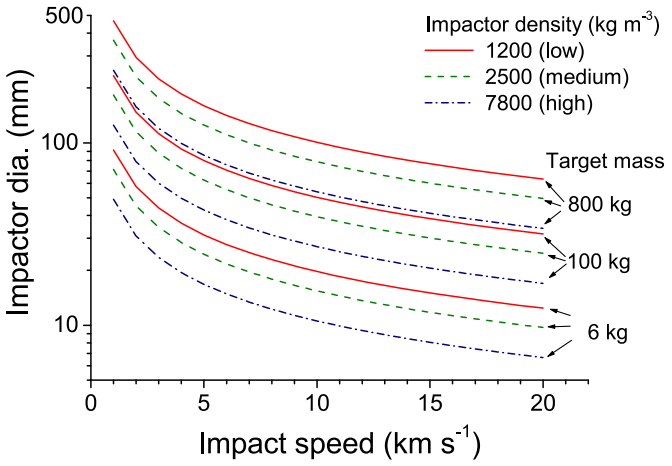


Fig. 2. Minimum impactor diameter to cause catastrophic disruption as a function of impact speed. Three sets of curves are shown for various target masses, with each set having three curves corresponding to low, medium and high density impactors.

Table 3
Impactor diameter (mm) just sufficient to cause catastrophic disruption calculated at a given impactor density and speed. In each case three values are given a/b/c, the left hand value is for a 6 kg target mass (e.g., a 3U cubesat), the central value is for a 100 kg target mass (e.g., that of the main bus for a OneWeb satellite) and the right hand value for a 800 kg target mass (e.g., a complete Starlink v2 satellite).

Impactor density (kg m^{-3})	Impactor Speed (km s^{-1})		
	5	10	15
1200 (low)	31/80/160	20/50/101	15/38/77
2500 (mid)	24/63/125	15/39/79	12/30/60
7800 (high)	17/43/86	11/27/54	8/21/41

For micron-sized impactors, the flux in LEO is sufficient for small area detectors to produce data in periods of a year or less. For larger objects, e.g., 1 mm diameter, the expected flux is of order one impact per m^2 per 78 years in LEO at 800 km altitude (a popular altitude), rising to 1 per m^2 per 3030 years for a 1 cm impactor (see Table 1 in Ref. [2]). This means that a large area, long duration mission is needed to measure the flux in-situ at these sizes, and none are currently operational. Furthermore, whilst these values suggest a low risk per spacecraft (even when the surface area of a that spacecraft is considered), the total risk requires that all spacecraft in LEO have to be factored in (which, as already stated, now exceeds ten thousand). Consequently, it is reasonable to state that impacts in LEO by objects large enough to potentially cause serious damage may be occurring every year. Fortunately, as yet they are not frequent enough to strike with high probability the smaller satellites more at risk of catastrophic disruption due to their low mass.

Given that the number of satellites in orbit is increasing rapidly, the measurement of the flux of mm – cm impactors is critical, both to determine what it is for flux modelling, and to see if it is growing with the increased use of space. Yet the measurements in this size range suffer from data gaps, or are based on extrapolations from old data sets. This is because the method of measuring this flux in the 1980–2010 period, used large surfaces (or indeed whole spacecraft) retrieved from orbit by the now-retired Space Transportation System (STS), see Ref. [51] for a discussion. In determining the flux impacting the retrieved exposed surfaces, the impactor size is estimated from the size of the impact feature, but its orbit, impact speed and date of impact are all unknown (although some assumptions can be made if the pointing history of the surface is known). The impactor composition can be found from detailed analysis of the impact feature, searching for impactor residue. This has difficulties however. In the 1990s, for example, such analyses often lacked sufficient sensitivity to find the small quantities of residue present, with typically only some 50 % of craters having detectable impact residues. Then, when this improved with more sensitive analytical instruments, the issue became one of correctly identifying the residue as impactor material vs. target material or contamination introduced during post-flight handling and sample preparation for analysis [51]. Thus, whilst the total flux of large (1–10 mm) impactors may be well measured in such work, there are difficulties with assigning impacts to the correct debris or cosmic dust category. Worse, the fluxes rely on just a few measurements, which, although made at discrete times after various STS mission (the last ending with the return of materials from the HST in 2009 by STS-125), used surfaces exposed for multi-year periods (those returned by STS-125 had been in orbit for 15 years) making it difficult to spot trends with time, and none have occurred since 2009.

1.7. Large area thin film dust detectors

With attention increasingly focused on the danger of HVI's in LEO, which can cause loss of control of a spacecraft or its catastrophic

disruption, it is unfortunate that there is a data gap in the critical mm to cm size range [2]. The need is thus for new, large area, in-situ detectors which can send data back to the ground without the need for retrieval. Several technologies exist, or are being proposed to measure the dust flux in LEO (e.g., see Table 2 in Ref. [50]). To meet this need, NASA developed the Space Debris System (SDS, see Ref. [52]. This was a 1 m^2 active area thin film detector. It used polyvinylidene fluoride acoustic sensors mounted on 25 μm thick Kapton films arranged in two layers separated by 15 cm. The acoustic sensors were used to find the time and location of the impacts on each layer (and hence the direction of flight), with impact speed obtained from the time of flight between the layers (with direction and speed providing an estimate of the orbit). The impactor size was determined by the magnitude of the acoustic signals. The method is described in Ref. [27] and similar results with 12.5 μm thick Kapton films are shown in Ref. [28]. Unfortunately, the SDS failed on-orbit, some 26 days into its 3 year mission [53]. Thus, whilst it showed that impact signals could be detected in space, the particles detected were only in the size range of some 30–110 μm due to the short data collection time. Furthermore, none penetrated to the second layer and hence no impact speeds were obtained.

Various schemes have been proposed to improve the acoustic sensing methods of the SDS, such as adding light flash detectors to the instrument suite (e.g., Refs. [54,55]), but several problems remain. The first is that 1 m^2 is still a small detection area given the expected flux at 1–10 mm sizes in LEO. This can be solved by using a larger exposed area, and proposals such as ESA's SAILOR/OPTIMIST mission would extend the surface area of an instrumented Kapton sail to some 25 m^2 [29]. Thus, effectively, a large area solar sail would be used as a detector, instead of as a means of propulsion as it was with, for example, the JAXA IKAROS [56] and the NASA ACS3 [57] solar sails.

Then, whilst the mean size of the impactor can be determined by an instrument with acoustic sensors, the shape cannot, and as indicated this is important when assessing the threat of debris. The shape will influence the signal of an acoustic sensor by changing the hole size in the impacted thin films. In the case of mm-sized spherical impactors, the hole in the thin film is circular and of the same diameter as the impactor to within a few % (e.g. see Fig. 10 in Ref. [28]). It is not clear, however, what shape is left by other impactor shapes, or how well this tracks the cross-sectional area of the particle. The SAILOR/OPTIMIST proposal [29] would determine the particle shape by optically imaging the larger holes in the thin films used in the detector (a complicated process given the large surface area of the films and the small hole size). However, this still assumes that the hole shape reflects impactor shape.

In the rest of this paper, therefore, a series of impact experiments on

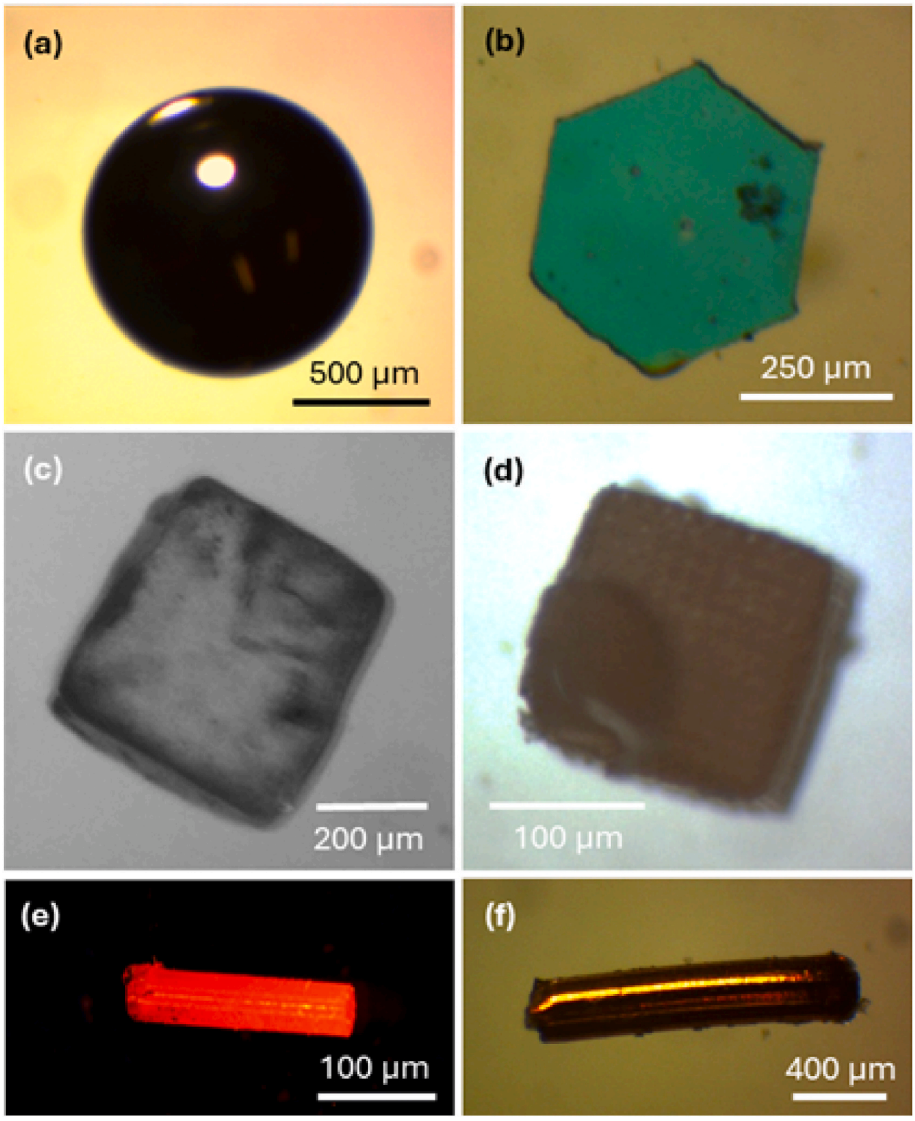


Fig. 3. Images of projectiles used in this work. (a) Sphere (1 mm, st. st.), (b) hexagonal polyester platelet, (c) sodium chloride salt cube, (d) resin cube (3D printed from Smoky Black Elegoo water washable resin, (e) resin rod (3D printed Tough Orange Prusament resin), (f) copper rod.

thin Kapton films are reported for a range of impactor shapes (sphere, cube, rod and platelet).

2. Experimental method

The DebrisSat experiment reported 6 main fragment shapes (straight rod, flat plate, flexible, bent rod, nugget, bent plate) from the breakup of the target satellite used in the impact test (Table 2). The work reported here used rigid shapes, so did not include any examples from the flexible category, and the influence of bent shapes is also left for later study. The shapes chosen for this work were therefore metal spheres (Fig. 3a), flat hexagonal polyester platelets (length:width of 12.5:1, see Fig. 3b), cubes of sodium chloride (NaCl) salt, and photopolymer resin (Fig. 3c and d) as example nuggets, and copper and resin rods (length:width of 4.5:1 to 5.5:1, see Fig. 3e and f). The sizes and compositions are summarised in Table 4.

The spheres (Fig. 3a) were sourced from specialist suppliers. The platelets (Fig. 3b) were commercial products widely available as sparkling glitter. Note that the ratio of internal widths on a single platelet varied by typically 1.2:1, slightly larger than for a regular hexagon (1.15:1). The salt (NaCl) cubes (Fig. 3c) were selected by size and shape from commercial salt. The resin cubes and rods were 3D printed using a Prusa SL1S SPEED printer (https://www.prusa3d.com/product/original-prusa-sl1s-speed-3d-printer-3/). The resin samples were printed in layers and cured using UV light. The resin cubes (Fig. 3d) were printed using Smoky Black Elegoo water washable resin, with a UV curing time of 35 s for the first few layers and 3 s for the subsequent layers. Tough Orange Prusament resin was used for the 3D printed rods (Fig. 3e). The metallic rods (Fig. 3f) were cut from commercial copper wire.

The shots were performed using a two-stage light gas gun at the Univ. of Kent [58]. The gun (see Fig. 4) uses a shotgun cartridge to drive a nylon piston down the first stage of the gun. This piston compresses a light gas (here hydrogen) which is sealed in the barrel in front of the piston by an aluminium bursting disk (which separates the initial barrel from a rifled launch tube). When the pressure in the hydrogen exceeds the strength of the bursting disk, it suddenly ruptures, releasing the highly compressed gas into the launch tube where a sabot is placed which houses the projectile. The sabot was made of isoplast (so it can slide easily down the launch tube) and was constructed from four interlocking pieces, with a hollow central shaft where the projectiles are placed.

Although the four pieces of the sabot are initially held in place while travelling down the launch tube, once the sabot exits the launch tube into the larger diameter range of the gun, the sabot parts separate laterally releasing the contained projectile which remains on the central axis of flight. The sabot parts are then intercepted using a thick metal stop plate (which has a central hole to permit the on-axis projectile load to continue on into the target chamber). The range of the gun and target chamber were kept under vacuum during a shot, typically 0.5–1 mbar, to prevent deceleration in flight. The shot speed was obtained from two lasers mounted transverse to the flight path between the stop plate and target chamber, and focussed onto photodiodes. Interruptions to the photodiode signals provided timing, which combined with the known lateral separation of the two lasers (499 mm), is sufficient to give speed to ±1 %.

The targets were pieces of 12.5 μm thick Kapton film, typically of surface area 8 cm by 8 cm, and of density 1420 kg m^{-3}. In one shot a larger piece (18 cm by 18 cm) was used in case the projectiles had spread out by the time they reached the target chamber. A fresh piece of Kapton was used in each shot. The speed of the acoustic wave in the Kapton has been measured previously as 1875 ± 25 m s^{-1} [28]. Behind the Kapton target was a 25 cm space, followed by several layers of paper in front of a thick metal target. The paper acted as a capture cell to slow impactors before they reached the final metal target and to prevent ejecta from the metal target travelling back towards the Kapton and causing more damage to it. Details of the shots are given in Table 5.

After a shot, the Kapton film was dismounted and imaged using a Leica optical microscope to find impact features. The lengths quoted in the measurements were regularly checked against calibrated scales for accuracy.

3. Results

Eight shots were performed in total for this work (Table 5). Impacts on the Kapton were produced for each type of impactor and typical hole shapes are shown in Figs. 5–9. Details of the holes made by each shape of impactor are given below and summarised in Table 6.

3.1. Spheres

The holes from impacts by spheres (Fig. 5a and b) were (1.004 ± 0.002) mm in diameter at 4.95 km s^{-1}, and (1.002 ± 0.004) mm at 5.22 km s^{-1}. They were circular to a high degree with no sharp corners (when measured multiple times the standard deviation on the individual diameters was 0.4 % at 4.95 km s^{-1} and 1.0 % at 5.22 km s^{-1}). Given the projectiles were 1.000 ± 0.008 mm, this means the holes were just under 0.5 % larger than the mean size of the projectile. This is similar to the results of [28], who found that the hole and projectile diameters for 25 μm thick Kapton impacted at 2 and 4 km s^{-1}, agreed to within 1 %.

The edge of a hole made by a spherical impactor can be seen in detail in Fig. 5c. The Kapton appears melted with small amounts attached at the rim of the hole. There is no significant amount of material folded back from the area of the hole, nor are there any radial cracks around the hole. The dark region of Kapton which lines the hole extends typically 9–10 μm beyond the rim of the hole itself, suggesting that damage may be confined to this region around the rim of the hole.

3.2. Platelets (glitter)

The effects of using thin, platelet projectiles (made of glitter) can be seen in Figs. 6 and 7, with impacts at 3.23 and 5.09 km s^{-1} respectively. A variety of hole shapes are evident, ranging from shapes similar to the platelets seen face on (e.g., Fig. 6a and b) to more elongated, relatively narrow slit-like holes, suggesting more edge on impacts (e.g., Fig. 6c–f,

Table 4
Projectile shapes used in this work.

Shape Name	Composition	Associated image	Size (mm)	Ratio of axes
Sphere	Stainless steel 420	Fig. 3a	Dia.: 1.00	1 : 1
Platelet (hexagon)	Polyester	Fig. 3b	Largest width: 0.45–0.55. Thickness: 0.04.	12.5 : 1 (average)
Cube	Salt (NaCl)	Fig. 3c	Average: 0.45 × 0.44 × 0.48, Individual cubes can vary by ±15 %,	1 : 0.98 : 0.94
Cube	Resin (Prussian)	Fig. 3d	0.70 × 0.69 × 0.68	1 : 1
Rods	Resin (Tough Orange Prusament)	Fig. 3e	Length 1.48–1.86 Width: 0.37	4.5:1 (average)
Rods	Copper	Fig. 3f	Length:1.07–1.45. Width: 0.23.	5.5 : 1 (average)

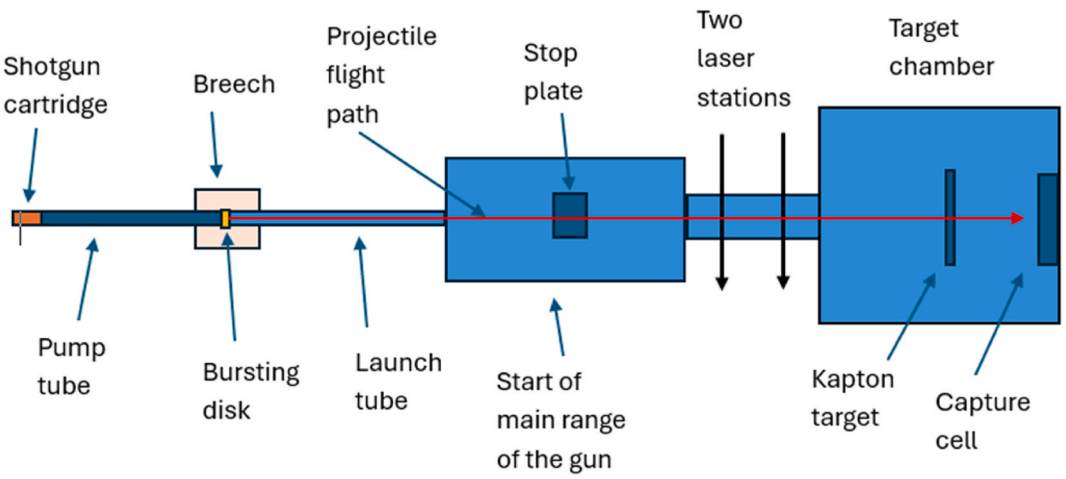


Fig. 4. Schematic of Kent two-stage light gas gun. In operation, a shotgun cartridge (left) is ignited and drives a nylon piston down a pump tube. The right-hand end of the pump tube is sealed by a bursting disk of aluminium, and the tube is prefilled with hydrogen. As the piston advances it pressurises the hydrogen to a high enough pressure to suddenly rupture the bursting disk. This releases the hydrogen at high speed into the rifled launch tube. The connection between the pump and launch tubes is surrounded by a breech to prevent gas leakage. At the left hand end of the launch tube, a four part sabot (made of isoplast) is placed – this contains the actual projectile placed in a hollow central shaft in the sabot. The launch tube and subsequent range of the gun are evacuated to approx. 0.5–1.0 mbar pre-shot. The sabot spins as it proceeds down the rifled launch tube, and when it enters the wider main range of the gun, the sabot parts travel off-axis and are intercepted by a stop plate which has a central hole to permit the projectile to proceed to the target. Two lasers (with a known lateral separation) are then mounted transverse to the projectile direction of flight and are focussed onto photodiodes to provide timing and spatial information necessary for speed determination. The projectile passes through the Kapton target in the target chamber and is then stopped in the capture cell on the far right.

Table 5
Shot parameters in this study. The targets were 12.5 μm thick Kapton films.

Shot No.	Speed (km s^{-1})	Projectile
1	4.75	1 mm st. st. sphere
2	4.88	Three cubes (NaCl)
3	5.09	Multiple platelets (hexagon)
4	3.23	Multiple platelets (hexagon)
5	5.22	A 1 mm st. st. sphere and multiple platelets (hexagon)
6	4.70	Three cubes (resin black)
7	4.95	A 1 mm st. st. sphere + four copper rods
8	4.59	Four 3D printed rods

Fig. 7). Clear corners with both large and small internal angles can be seen. For example, in Fig. 6a, the internal angles ranged from 120°–150° (compared to 120° for regular hexagons). In Fig. 6b, most internal angles range from 130° to 145°, but there was one sharper corner with an internal angle of 75°. In Fig. 6c and d, the shapes are more oval (or ellipsoid), with rounded ends. However, in Fig. 6e and f and Fig. 7, there are sharper corners present, with internal angles around 90°. Indeed, in Fig. 7, the sharper end of the slit-like hole has an internal angle of 50°. This range of internal angles suggests that where all are just slightly above 120° a face on impact has occurred (Fig. 6a), and when some smaller internal angles start to appear, a more edge on impact has taken place. Then, as the corners become sharper and more acute, the platelet is impacting even closer to edge on.

No examples of very narrow slit-like holes were observed. The ratio of hole length:width is typically some 2.5:1 to 3:1, which is much less than the ratio of length to thickness for a raw platelet (12.5:1, see Table 4). Given the limited number of holes observed, it is not clear if this is due to the absence of any edge on impacts, or if the Kapton does not preserve shape at such extreme ratios (also see section 3.4 for the results of impacts by rods). However, it can be seen in Fig. 6, that in case of slit-like holes, the Kapton has not been aways been melted away or clearly punched out, there are several large pieces of Kapton which have been folded away and are still attached at the hole edge. This does not appear to be happening in Fig. 7 (i.e., at the higher speed of 5.03 km s^{-1}), although there are fewer examples to examine. Instead, the long slit-like hole in Fig. 7 (which has the longest length:width ratio observed) has stated to rise on the right side of the hole and a tear has begun to form. This suggests that, as well as impactor shape, there may be some impact speed related effects occurring which influence folding and tearing vs. melting.

The longest dimensions of each hole in Figs. 6 and 7 were measured. In Fig. 6a–f these were 465, 620, 558, 697, 543 and 775 μm respectively, and 625 μm in Fig. 7. Given that some of these values exceed the size range for the raw platelets (450–550 μm) this suggests that the main axis in the holes can be slightly longer than that of the impactor. The notable exception is Fig. 6a, which the evidence suggests is a face on impact that is within the expected size range (and whose cross-sectional area is thus within the range expected for a raw platelet). For better comparison of the hole and projectile sizes, Fig. 7 shows a hole with a piece of raw glitter platelet placed on the microscope stage behind the Kapton film (the faint glitter image is outlined in white to aid visibility).

As stated in Table 4, the mean maximum internal diameter of an individual raw platelet is 0.5 mm (Table 4), which gives the area of the flat surface of a raw platelet as typically 0.16 mm^2. Given that the width of the hole in Fig. 6a is compatible with that of the face of a typical platelet, its area also corresponds to that of the flat face of one of the projectiles. However, if we approximate the slit-like hole in Fig. 7 as an ellipse, then its area is 2/3 that of the flat surface area of a typical piece of the raw glitter. Similarly, if we take the longest slit observed (Fig. 6f) and find its area by approximating it with a set of squares and triangles to fill the space, then the area is 0.26 mm^2, i.e. larger than expected. Since the orientation at impact is not known, it is not clear how well the holes represent the cross-section of the impactor as it passed through the Kapton film. Nevertheless, the hole areas span a range of 0.67–1.62 times the area of an average flat platelet.

3.3. Cubes

Two types of cube were used in this work. The first were crystals of NaCl (common table salt), where several cubes were fired in a single shot at 4.88 km s^{-1}. Based on the holes in the film post-impact, only one cube reached the target intact (the hole is shown in Fig. 8a). The other cubes seem to have broken up during launch and sprayed the Kapton film with a large number of smaller impactors, producing many small holes. The

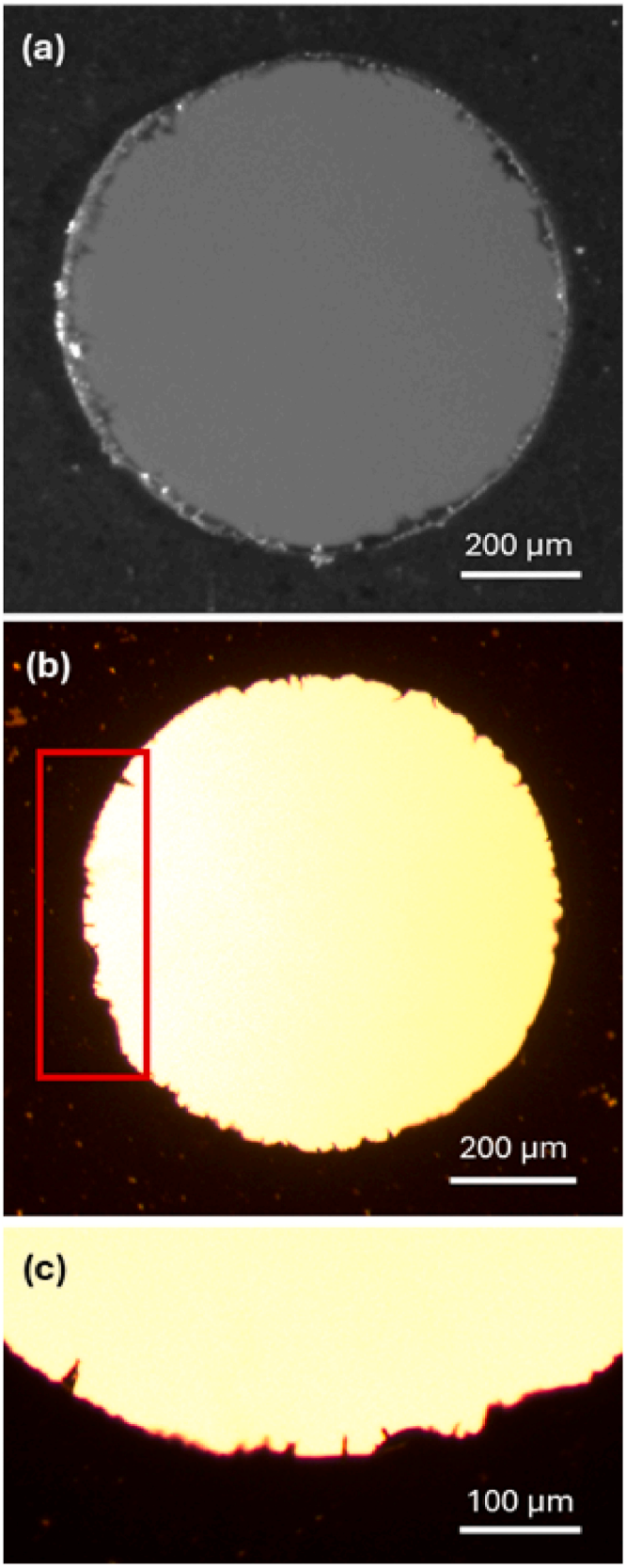


Fig. 5. Images of holes in Kapton foils created by spheres (a) 5.22 km s^{-1} (top illumination), (b) 4.95 km s^{-1} (rear illumination). The left-hand part of the rim of the hole that is highlighted in a rectangular box is shown on an expanded scale in (c) to show the detail of the hole edge.

large hole (shown outlined in Fig. 8b) has six straight edges with clear corners, very different to the circular rim from a spherical impactor. The internal angles at the corners range from 90° to 150°. The shortest and longest sides have a length of 84 and 382 μm respectively, and the maximum internal width orthogonal to the longest side is 262 μm. Given that individual cubes could vary in size by ±15 % (see Table 4), the maximum length here is compatible with the edge length of a small NaCl cube pre-shot, but all other dimensions are smaller. The area of the hole was 0.103 mm^2, compared to 0.146 mm^2 which is the area of one face of a cube with sides 0.382 mm.

Since several of the NaCl cubes had broken up during launch, it is possible the hole in Fig. 8a, was made by a large fragment of a cube, rather than by an intact small cube, and this would explain the smaller than expected dimensions. Given that the material properties of the NaCl cubes lend towards breakup during acceleration, it was decided to use 3D printed cubes for further shots. A shot was made at 4.70 km s^{-1}. Two cubes reached the target, producing the holes shown in Fig. 8c and d. Both holes are distinctly non-circular, with corners visible, and in both cases part of the Kapton has folded back from the hole.

The hole in Fig. 8c has clear corners, but is not at first glance a clear reflection of any particular aspect of a cube. The longest axis in the hole has length 1188 μm, and transverse widths typically range from 650 to 760 μm. The shortest widths are on the side where a fold of material appears to obscure the true edge of the hole (marked by the right-hand arrow in Fig. 8c), thus the smallest width may be slightly larger than stated. By geometry, for a cube of side L, the longest internal diagonal is $\sqrt{(3)}$L. Here, given L for the 3D printed cubes is typically 690 μm, the longest internal length in a cube is approximately 1190 μm. Thus overall, the dimensions are compatible with passage of a cube through the film. Similarly, the hole in Fig. 8d has a largest visible dimension of 1179 μm (slightly longer than the expected largest internal dimension of one of the cubes) and a transverse width which is again hard to estimate (again due to the presence of a fold of Kapton obscuring one side of the hole) but is approximately 790 μm. This is again consistent with passage of a cube through the film which has torn and folded the Kapton in the region of the hole.

3.4. Rods

A hole made by a copper rod at 4.95 km s^{-1}, is shown in Fig. 9a. The hole is neither circular (as might be expected for exactly head on impacts) nor rectangular (as expected from sideways on impacts). Instead it has a long main axis (310 μm) which is shorter than the length of a typical rod (1070–1450 μm, see Table 4), and a narrower transverse axis (230 μm at its widest) which is compatible with the expected 0.23 mm width of a copper rod. The width is not constant, however, and narrows at one end. Examination of images of the rods taken pre-shot, showed that, as can be seen at the left end of the rod in Fig. 3f, there can be a degree of pinching of the rod at one end as a result of the cutting technique used. This can result in a pointed end of the rod, and in the worst case, this pinching extended about 15 % of the length of the rod.

If the length of the longest axis of the hole reflects the orientation of the rod at the moment of impact, the hole in Fig. 9a suggests an impact at 73°–78° to the Kapton surface (defined by the orientation of the longest axis of the rod with respect to the planar surface of the Kapton film). In Fig. 9a, it is suggested one end of the rod struck the Kapton first, giving the squarish shaped end of the hole, and the rest of the rod then passed through the Kapton.

The shot with the 3D printed rods produced one hit (Fig. 9b). The hole has a clear edge on one side, but on the other side the displaced Kapton is still connected to the main body of Kapton. It has started to raise from the surface and the free edge has started to fold back on itself. There are crack-like fractures continuing into the Kapton from the edges of the hole (shown circled in Fig. 9b). The length (longest axis) of the hole is 753 μm. The width (the direction transverse to the length) is harder to measure as it depends on where the Kapton has started to be

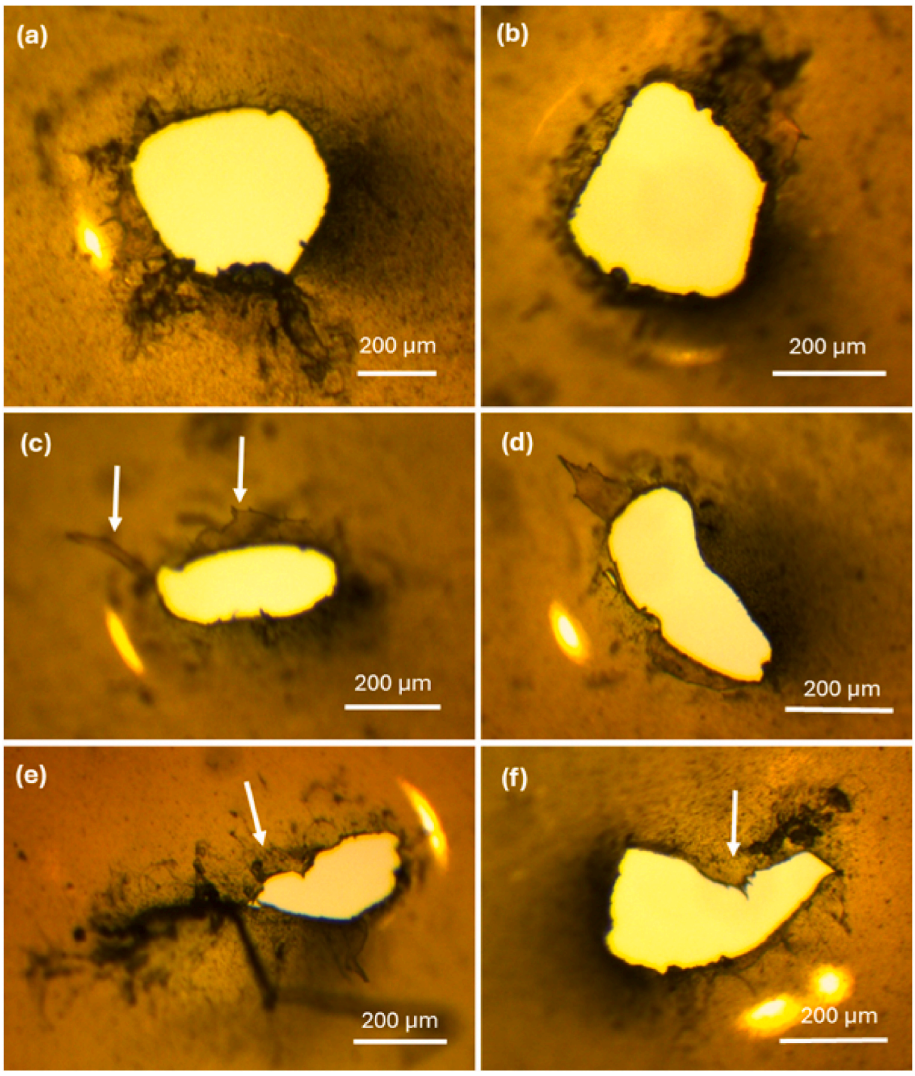


Fig. 6. Images of holes in Kapton made by platelet (glitter) impactors at 3.23 km s^{-1}. All images are of the front face of the Kapton. (a,b) show large area features with sharp corners, broadly similar in shape to a piece of raw glitter (see Fig. 3b), suggesting near planar impacts. (c–f) show long, narrow holes, suggesting more edge on impacts have occurred. In (c) and (d) long stands of Kapton are visible (see arrows), attached at the hole edges, suggesting the Kapton was not removed by melting but tore and folded back during the opening of the hole. The holes in (e) and (f) have very irregular shapes, suggesting that part of the folded Kapton (shown arrowed) may have relaxed back into the hole region after the impact (which may also explain the inward curvature of part of the rim of the hole in (d)).

raised from the original surface. In effect, a judgement has to be made as to where hole ends and the cracks begin. Based on this the hole width is some 320–400 μm. This range is compatible with the width of the rods (370 μm). Based on the hole length compared to the length of the original rods (1.48–1.86 mm), it is likely the inclination of the longest axis of the rod at impact was 59°–66° to the surface of the Kapton.

4. Discussion

4.1. Implications for predictions of impactor size

Most flux estimates in space present a dust flux vs. either particle size (radius or diameter) or mass. In the case of spherical particles of common density, this is not a particular issue, as radius, diameter and mass are all readily convertible. This is not the case here for non-spherically shaped objects of different compositions (and hence densities). Treating density first, the data in Table 2 shows that a wide range of densities are to be expected when observing orbital debris. This issue has long been recognised and represents a difficulty in relating observed sizes with likely masses. Thus presenting flux curves vs. object size (which is often more easily estimated) is a sensible response.

However, when objects are of various shapes, a new issue arises - what size characterises an object? The radius of the sphere of equivalent volume was a traditional choice. This is not a bad approximation for objects like natural cosmic dust, which are mostly spherical or ellipsoidal with, at worse, a ratio of the longest to transverse axes of 2:1 [59]. In the case of orbital debris, this does not hold. The issue of how to characterise the size of orbital debris predicted from the DebriSat experiment is discussed in detail in Refs. [36,31] for example. The complications arise from the wide variety of shapes, each of which can have a range of relative dimensions. For example, the DebriSat experiment reported rods which had length to width ratios of greater than 4:1, and platelets with the shortest axis less than 1/16 × the largest, and used a characteristic length which was the average of all three main dimensions of an object [36].

In the results here, this is further complicated as the hole in a thin film only provides a 2D projection of the geometric cross-section of an object, in the aspect at which it passed through the film. Therefore, even though the hole shape is representative of the impact event, separating the impactors into shape classes based on the hole is not a one-to-one mapping issue. It is possible here because the shapes used in each shot were known, but in space this will not be the case. For example, is a slot-

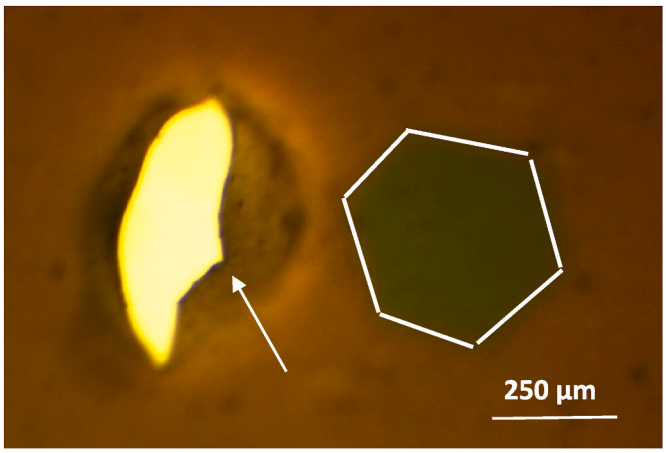


Fig. 7. Comparison of hole size in Kapton (at 5.09 km s^{-1}) with piece of raw glitter. The glitter was placed behind the Kapton on the microscope stage and to make it more visible its outline has been traced in white. The maximum width of the piece of glitter well matches the maximum length of the hole, but the transverse width of the hole is much less than any similar dimension in the raw glitter, suggesting a near side-ways impact occurred. On the right hand side of the hole the Kapton appears slightly elevated away from the original surface, and a tear has started to appear (shown arrowed).

like hole due to sideways passage of a rod, or an edge-on impact of a platelet? Even the case of a circular hole does not have a unique origin, it may be caused by passage of sphere, or by a fortuitous end-on impact of a rod of unknown length. Turning the observed hole area into a characteristic length, or even shape, is thus a task that will involve assumptions by the user, and these assumptions will carry associated uncertainties. Nevertheless, although exact shape categorisation will not be possible, it has been shown here that dividing holes into those likely to be caused by more spherical vs. less sphere-like objects will in general be possible.

4.2. Hole size predictions and ballistic limit thickness

There have long been parameterisations available predicting the size of holes from impacts by spheres on thin films, e.g., Ref. [60]. A detailed parametrization of hole size and comparison to data and earlier models is given in Ref. [15], for example, but most earlier work was for impacts on metal targets. However, in Ref. [61] Neish et al., data are shown for impacts, at 5 km s^{-1}, of glass beads (diameters 57–400 μm) on Kapton films of thickness 7.5–175 μm. They measured hole diameters in the Kapton and found that they were always larger than the projectile diameter by a factor typically 2.2 when the projectile diameter was between 0.3 and 5 times the target Kapton thickness, but that hole and projectile diameters converged when the projectile was >10-20x the target thickness (see Fig. 10 in Ref. [61]).

Subsequently, Neish and Kibe (see Ref. [62]) considered impacts on Kapton films (thicknesses 25–175 μm) and derived an expression of the form:

$$d/T = 0.337 + H/T \times \left(1 - 0.8912^{(d/T+0.06502)}\right) \quad \text{eqn. (1)}$$

where d is projectile diameter, H is hole diameter (measured in the original surface plane of the film, i.e., not the lip to lip diameter that is often used for crater measurements), and T is film thickness. As long as d, H and T are in the same units, this is a dimensionless relationship. Note that [62] averaged over projectile composition (i.e., density and strength) and impact speed. Thus eqn. (1) should thus be taken as illustrative, rather than definite for any specified impactor composition and speed. However [61], did validate their relationship against experimental data for impacts on Kapton of spherical glass beads (diameter of 57–400 μm impacting at 5 km s^{-1}), similar to sizes and speeds of interest here. The results of eqn. (1) are shown in Fig. 10, in the traditional form where both projectile and hole diameters are normalised to film thickness. The data that [62] compared to their model, sits in

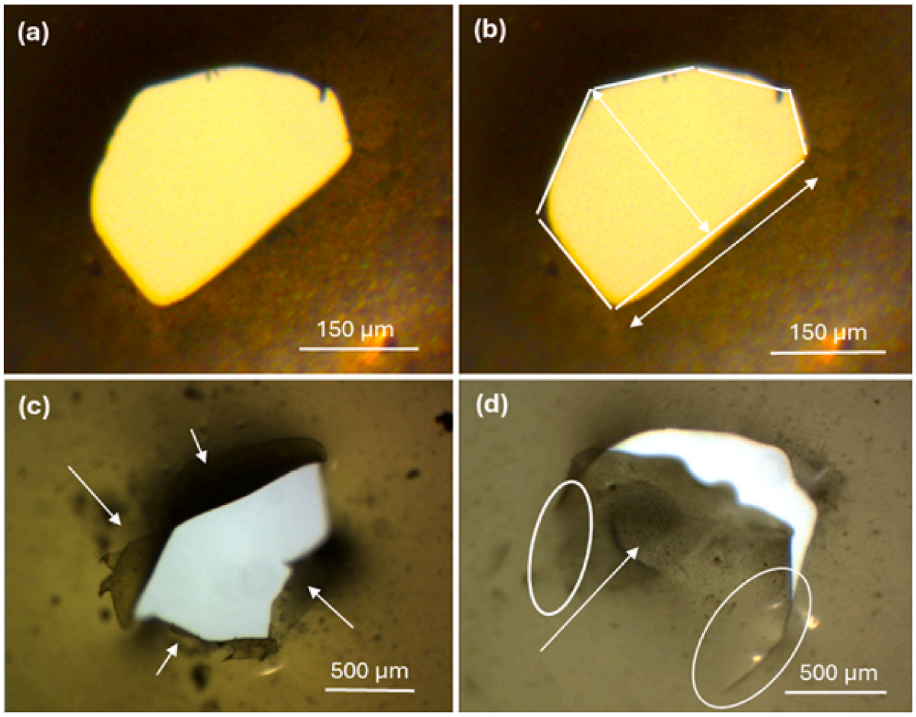


Fig. 8. Images of holes in Kapton by cubes. (a) Sodium chloride salt cube at 4.88 km s^{-1}. This is shown again in (b), with the hole outlined with white lines. There are 6 straight edges, and the longest length and the axis orthogonal to this are marked with arrows. (c,d) Holes in Kapton from impacts by black resin cubes at 4.70 km s^{-1}. Areas of torn Kapton which has been folded away from the hole are marked with arrows. In (d) a single large piece of Kapton has been torn and folded back (shown arrowed), with tears extending into the Kapton away from the hole (shown circled).

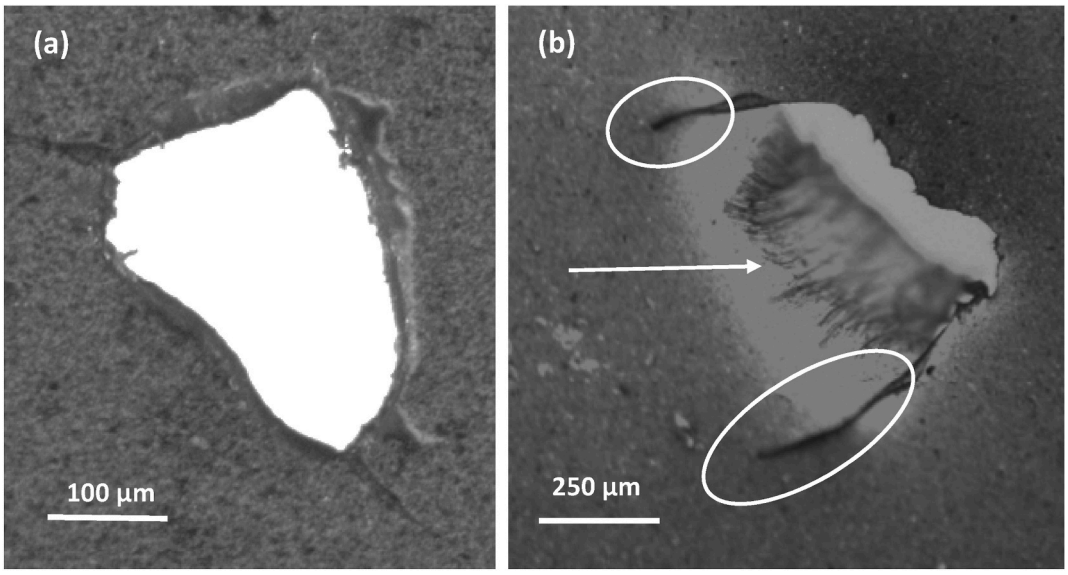


Fig. 9. Images of holes by rods. (a) Impact by a copper rod at 4.95 km s^{-1}. The hole is 310 µm (longest axis) by 230 µm (transverse width). (b) Impact by a 3D printed resin rod at 4.59 km s^{-1}. In (b), a large raised region of Kapton is visible which has started to foldback on itself (shown with an arrow), cracks that extend away from the hole are also visible (circled). The longest dimension of the hole in (b) is 753 µm, but the width is uncertain, and depends on where the raised Kapton is taken to lift away from the original surface.

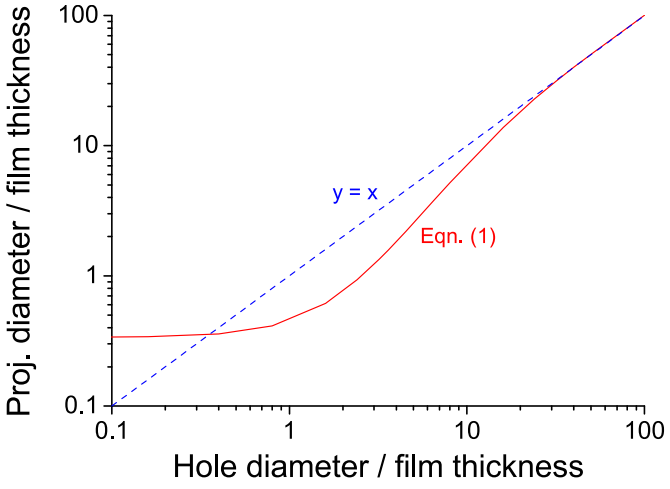


Fig. 10. Projectile diameter vs. hole diameter (both normalised to film thickness) for hypervelocity impacts on Kapton according to eqn. (1) (the case of y = x is also shown for comparison). For normalised hole diameters greater than 10, the normalised projectile and hole diameters converge, whereas at very low hole sizes the relationship breaks down to a constant projectile size given by the ballistic limit of the film.

the range 0.6–10 for the hole diameter/Kapton thickness. At larger values of the normalised hole diameter, the predicted particle diameter rapidly converges to the hole diameter, whereas at lower values the predicted hole diameter rapidly falls off towards zero, as projectile diameter decreases only slightly. This latter feature is somewhat artificial, reflecting that the ballistic limiting thickness of the film has been reached and no penetration is actually occurring, resulting in the absence of a hole.

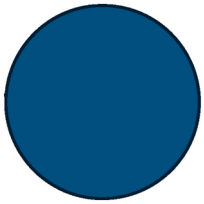
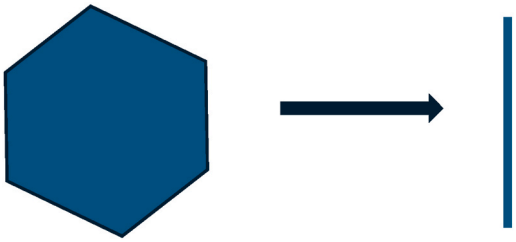
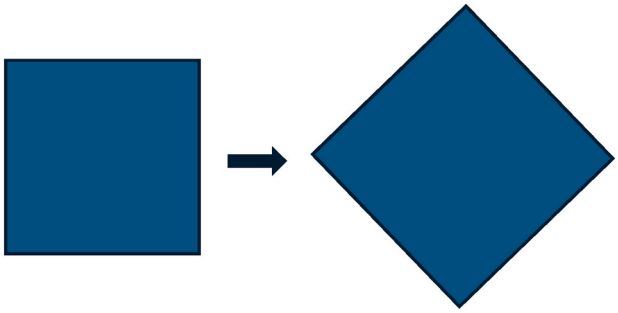
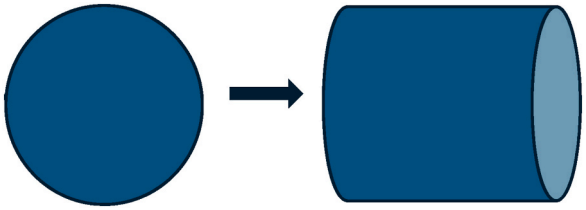
Traditionally, what are termed hole growth equations are cast in the form of eqn. (1), because it is the hole diameter (H) that is measured and the particle size (d) that is unknown. In the present case it is more useful to be able to predict absolute hole size as particle size varies, and this is done in Fig. 11 for several thicknesses of Kapton (5.0, 7.5, 12.5 and 25 µm, corresponding to typical sample thicknesses).

The relationships in Fig. 11 shows distinct regimes. As discussed in Ref. [15], at large projectile sizes compared to the film thickness (d/T » 1), the hole and particle sizes converge, with no damage occurring to the projectile during penetration; this is the Thin Film regime. At an intermediate scale, where d/T falls to a value of some 4 or 5, the particle diameter is smaller than the hole diameter and the impactor is in increasingly disrupted during penetration; this is the Transition (or ballistic) regime. Then as d/T tends falls to unity or less, the particle fails to penetrate and the impact produces a crater rather than a hole. Here the relationship in eqn. (1) fails. The critical impactor size which just penetrates is given by the ballistic limit (which strictly speaking refers to a speed required to penetrate a layer of material, but here is used to denote the target thickness for a given impactor size and speed). From Fig. 11, it can be seen that the projectile size that just penetrates is respectively some 1.7, 2.6, 4.2 or 8.5 µm, for Kapton thicknesses of 5.0, 7.5, 12.5 and 25 µm (see Table 7).

If thin Kapton films are used in space to detect dust impacts, the different responses to impacts in the three regimes are significant. Below the ballistic limit, micron and sub-micron particles effectively impact a semi-infinite target and a crater forms. Strictly speaking, to reflect this, the calibration of any sensor attached to the film will change above and below the ballistic limit (as differing amounts of the impact energy/momentum are retained in the target). However, the associated particle size below the ballistic limit will be less than a few µm, and such impacts may well be below the detectable limit if acoustic sensors are used. At larger particles sizes, penetration occurs, but, as stated above, initially the hole size (diameter) is larger than the impactor, typically by a factor of some 2.2 (and hole area by a factor of 4.8). It is not clear how this will affect the detection by any sensors attached to the thin film. If the sensor response depends on hole area for example, the results may overestimate the cross-sectional area of an impactor by a factor of nearly 5, as will analysis techniques based on imaging the hole. This is important given that smaller particles dominate the impactor flux in space, and it is only for holes above a few hundred µm (as in this paper) that the hole sizes will match impactor dimensions. Missions such as SAILOR/OPTIMIST [29], which intend to image the impact holes to determine impactor size, will need to take this into account.

Another factor to consider is the impact speed dependence of these results. The data here, and the formulism of eqn. (1), apply at 5 km s^{-1}.

Table 6
Diagrammatic representation of the range of hole shapes made by different shapes of impactors. Note that when corners are present, tearing and folding of the target thin film may also occur.

Projectile Type	Range of hole shapes	Comment
Sphere		Hole diameter similar to projectile diameter
Platelets		Hole shape ranges from face-on to side-on impacts
Cubes		Hole shapes range from side-on impacts (where length of sides equals L the length of sides of cube and the diagonal equals $\sqrt{2} \times L$) to corner-first impacts with diagonal length $\sqrt{3} \times L$
Rods		Hole width is fixed, but length varies from equal to rod width (end-on impact) to length of rod (side-on impact).

As shown in Fig. 1, higher speeds are likely for much space debris, depending on the inclination of the orbit in LEO. The work reported in Ref. [61] did attempt to determine a velocity dependence for hole size in the Transition regime data-region, suggesting $v^{-1.0671}$ (where v is in km s^{-1}). However, this was based on a different data set using multi-layer insulation (MLI) as the target and not the same raw Kapton material as was used to determine eqn. (1), and they noted that the results for hole size in the MLI were incompatible with those for the raw Kapton. This suggests that the result obtained should not be considered definitive and the correct impact speed dependence remains to be determined.

It is also possible to compare the results found here (for the parametrization specifically developed for Kapton, i.e., those from eqn. (1)), with those predicted for impacts on thin metal films. For example, analytic models (based on simple physics assumptions) have been developed to predict the ballistic limit (important for shielding) for impacts of orbital debris on thin metal sheets, e.g. Ref. [63]. In eqn. (20) in Ref. [63], the ballistic limiting thickness (h) for a thin metal sheet is given by:

$$h = (r\rho v / 4k_1)\left(1 + \sqrt{[1 + (8k_1\rho_2 L)/(\rho^2 v r)]}\right) \quad \text{eqn. (2)}$$

where r, L, ρ_2 and v are respectively the initial impactor radius, length, density and speed, ρ is the target density, and,

$$k_1 = \lambda\, \rho\, a_p \quad \text{eqn. (3)}$$

with λ being the friction constant and a_p the acoustic sound speed in the target. If the projectile is assumed to be soda lime glass (as before) and the target Kapton, the appropriate values for the density are ρ (Kapton) = 1420 kg m^{-3} and ρ_2 (soda lime glass) = 2500 kg m^{-3}. Taking $\lambda = 0.48$ for thin Kapton film [64], a_p is 1875 m s^{-1} (as determined in Ref. [28] for hypervelocity impacts on thin Kapton films) and the projectile as a sphere with L = 2r and v = 5 km s^{-1}, then h can be found for varying values of r. For Kapton sheets of known thickness (5, 7.5, 12.5 and 25 μm as before), the size of the projectile that just penetrates can be found and compared to that found earlier for these Kapton thicknesses in Fig. 11. The results are given in Table 7, where the predictions of the ballistic limit made using the formula developed for thin metal films (eqn. (2)) gives results similar to (albeit approximately 20 % greater than) those from the formula for Kapton given in eqn. (1).

4.3. Ductile vs. brittle response of the thin film

Early discussions (e.g. Ref. [65]) identified penetration of thin films

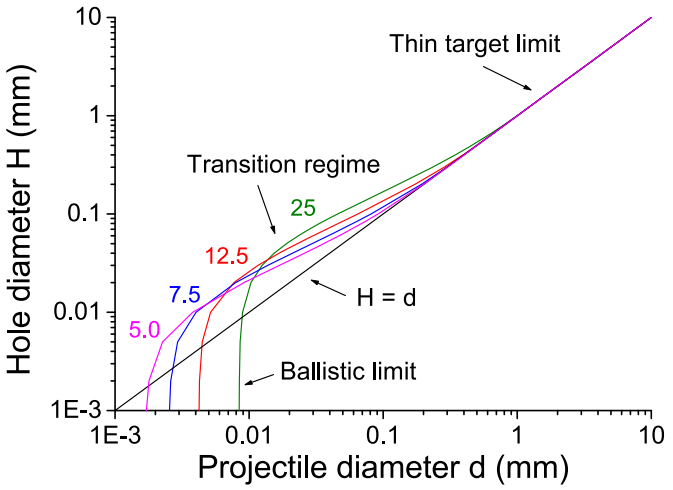


Fig. 11. Hole vs. projectile diameter for different Kapton thickness (5.0, 7.5, 12.5 and 25 μm as labelled on the relevant curves). At large projectile sizes (above approx. 0.2–0.5 mm) the hole and projectile diameters converge in the thin film limit. At very small projectile sizes (2–10 μm) the ballistic limit is reached, where no penetration occurs.

Table 7
Predictions of the diameter of spherical projectile at the ballistic limit for penetration of a thin Kapton film.

Kapton Thickness (μm)	Impactor diameter to just fail to penetrate (μm)	
	Kapton Parametrization Eqn. (1)	Thin Metal Parameterisation Eqn. (2)
5	1.7	2.1
7.5	2.6	3.1
12.5	4.2	5.2
25	8.5	10

as occurring due to shearing failure of the thin target which was treated as a visco-plastic solid. Damage mechanisms specific to thin films have been discussed by Ref. [66] (at speeds up to 3 km s^{-1}) and [67] (at 5 km s^{-1}), who both reported on the impacts of flyer plates on thin polyimide films. In Ref. [67], it was found that for impacts on thicker films (25 μm thick), the resulting holes in the film were slightly irregular, with raised lips which had just started to crack. However, for thinner films (12.5 and 8 μm thick) under similar impacts, radial cracks stated to propagate away from the hole, and increased in number and length as the film became thinner. They suggested this was due to the target film in the central hole region behaving as a ductile material, whereas in the surrounding material it behaved in a brittle fashion. This ductile behaviour would explain why a formula developed for penetration of ductile metal films (eqn. (2)) reproduces the ballistic limits predicted by the parametrization developed for Kapton (eqn. (1)).

Here, at around 5 km s^{-1}, the results show that, as previously reported (see Ref. [28] and discussions therein), smooth, rounded holes (Fig. 5a and b) are caused by spherical impactors at around 5 km s^{-1}. Close examination of the rim of the holes shows that some irregularly shaped material remains attached at the rim, and that this appears mostly melted (Fig. 5c). Then, as shown by the holes from non-spherical impactors, as the cross-sectional area of the impactor becomes less circular, radial cracks start to appear in the target film around the main hole, along with folding back of the displaced Kapton. Thus here, in a single thickness of kapton film, both behaviours are seen, dependent on the shape of the impactor and hence the hole. Where what are effectively corners are present in the edge of the hole (i.e., sharp changes in direction of the hole rim), the resultant stresses may cause fracturing of the target in a brittle fashion. However, if no such focus of the stresses is present, fracturing does not occur. Furthermore, the damaged area around the hole seems slightly different depending on whether the hole is circular or not. In the former case there is a relatively narrow discoloured region close to the rim of the hole, suggesting damage has occurred in this region. In latter case, folding back of the Kapton is more common with no well defined region of discoloured Kapton surrounding the hole rim.

4.4. Extent of damaged region of kapton around the rim of a hole

As stated, the impact hole that forms does not represent the limit of the damage zone in the Kapton film. This is particularly apparent for impacts by spheres. Conveniently, as noted earlier, the salt cubes used in the shot at 4.88 km s^{-1}, had a tendency to break up when accelerated in the gun, producing a shower of smaller projectiles that impacted near simultaneously. This is shown in Fig. 12, where many holes can be seen in the Kapton. These holes were mostly circular (or near-circular) with a diameter typically in the range 30–110 μm, and appear similar to those caused by spherical impactors.

Around a single such hole, a damaged region can be seen in the Kapton (e.g., Fig. 12a and b). For these small holes, this region extends typically 18 μm beyond the hole radius. This is almost twice as far as in the case of larger, 1 mm diameter holes made by spherical projectiles, suggesting there is a weak inverse dependence of the width of this region vs. hole size. When holes are close to each other, these extended damaged regions start to merge (Fig. 12c and d). When significant overlap of the extended damaged region has occurred, but before the actual holes themselves would have overlapped, the Kapton between the two holes breaks and a single hole is formed with a figure of eight shape (Fig. 12e and f). It is therefore suggested that this transition to a single hole occurs at, or close to, the case where the damage zone around one hole reaches the original perimeter of a second hole. When this happens, the piece of Kapton which would otherwise lie between the two individual holes, tears and folds back, connecting the two holes. This reinforces the idea that the residual damage to the Kapton after hole formation is limited to a relatively narrow region around a hole.

4.5. Impact energy density

As discussed in section 1.3, it is not clear what the impact energy is in cases where the target is a thin film and penetration occurs. For a 1 mm stainless steel projectile in shots here, the kinetic energy is some 51 J. For an 8 cm by 8 cm piece of Kapton (with mass of 99 mg), this would imply an apparent impact energy density of 510 kJ kg^{-1}, well in excess of both the 40 kJ kg^{-1} taken as Q^* (the catastrophic disruption limit) of a spacecraft and of the much lower Q^* values for solid materials (some 0.5–10 kJ kg^{-1}, see Section 1.3). However, for a thin film, the projectile penetrates the target, with only a minimal fraction of the energy being transferred to the film. Thus the actual impact energy density in the target is much lower by an unknown fraction. This holds for impacts in the thin target limit regime.

In the ballistic limit regime, where the full impactor kinetic energy transfers to the target (and any associated ejecta), the impactor size is on the micron-scale (or below), so the impactor kinetic energy is at least 9 orders of magnitude lower than here. In the transition regime, the impactor is smaller (10–100 μm) than the 1 mm example, and an increasing fraction of the incidence kinetic energy is transferred to the target as impactor size reduces. The smaller size reduces the kinetic energy by a factor of 10^3–10^6. Given that the estimates of Q^* for some materials are around 10^3 times smaller than the Q value associated with 1 mm stainless steel projectiles used here, then if a significant fraction of the kinetic energy were transferred to the target film, this could be an issue. However, as long as penetration is occurring, and the fraction of kinetic energy that is retained in the film is low, this explains why thin films deployed in space exhibit holes at impact sites rather than larger scale disruption.

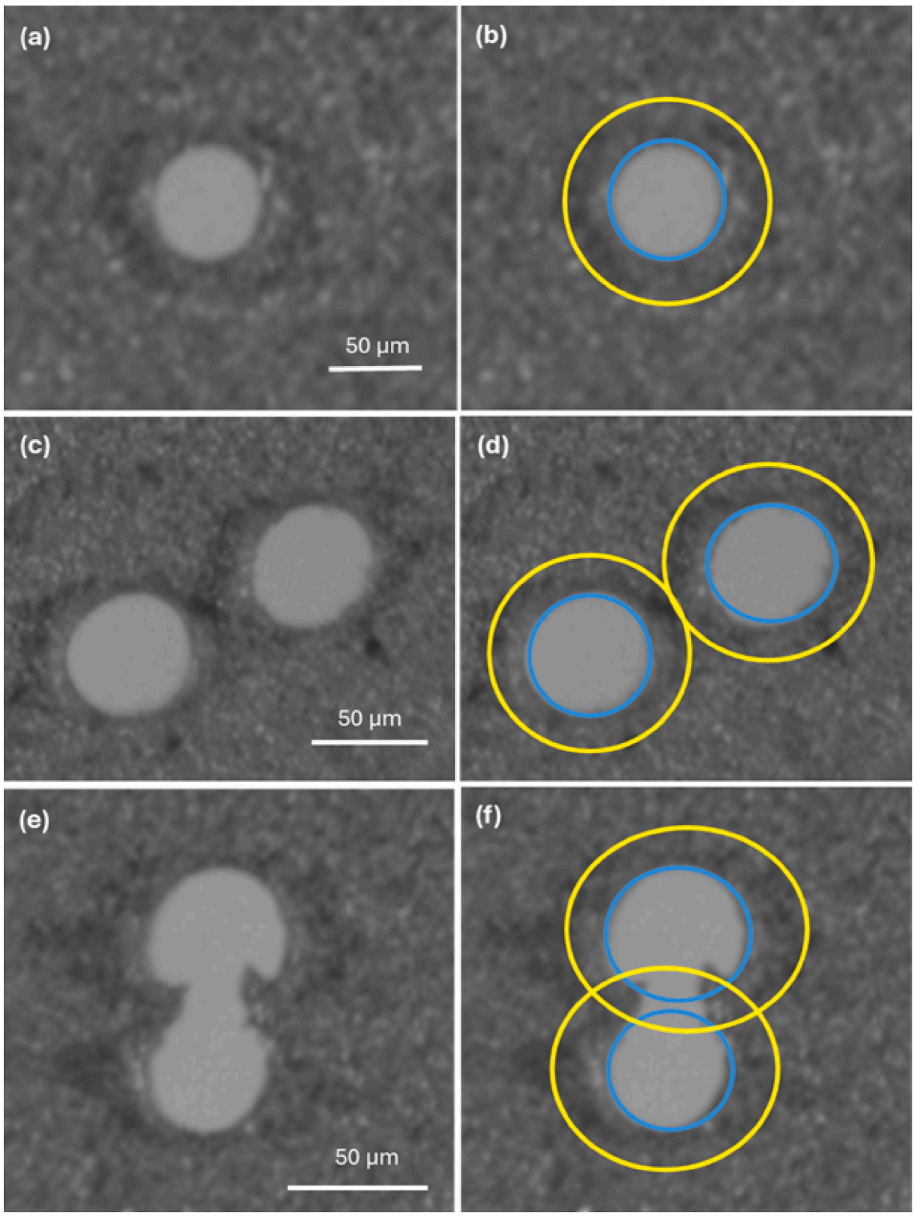


Fig. 12. Multiple small holes from impact of sodium chloride salt at 4.88 km s^{-1}. The left hand column shows (a) a single, isolated hole, (c) a pair of close neighbouring holes, and (e) a pair of just overlapping holes. The right-hand column (b, d, and f) shows the same images where an inner (blue) ring delineates the edge of a hole, and an oiuter (yellow) ring marks the edge of the damaged zone in the kapton surrounding the actual hole. Note in (e,f) that it is when the outer damaged Kapton zones start to significantly overlap, that the Kapton between the two otherwise still separate holes tears, and a single "figure of eight" hole is formed. (For interpretation of the references to colour in this figure legend, the reader is referred to the Web version of this article.)

5. Conclusions

The nature of impacts of debris on spacecraft in Low Earth Orbit means they occur in the hypervelocity regime. Here it is shown that different shaped impactors (corresponding to several of the more common shapes of orbital debris) result in different shaped holes in thin films from impacts at such speeds. The classic circular hole often reported in the literature (e.g., Refs. [28,54]) is thus a special case that strictly only applies to spherical impactors. In general, the presence of angular corners in the aspect of a non-spherical impactor presented in the impact, can be seen in the resulting holes, as can tears and large folds around the holes in the target thin film, both of which are absent from circular holes. The size of an impactor (as projected onto the surface of the thin film as it passes through) is mostly reflected in the hole dimensions; as expected given that the size of the impactors, relative to the film thickness, places the impacts in the thin film limit regime (Fig. 11). After an impact, the damaged region in the Kapton appears, for circular holes, to be confined to a narrow rim region around the hole of some 10–20 μm. By contrast, for non-circular holes, folding back of the Kapton and cracks often appears around the rim of the hole.

This has significant implications for impact detectors using penetration of thin films as part of the detection method. The first is that, for all shapes of impactor, the area of the impact hole reflects the area of the impactor as it passes through the film. However, unlike the case for spherical impactors, this area is not fixed just by the size of the impactor, but also by the cross-sectional area of the aspect it presents during the impact. Depending on the impactor shape this can represent a significant deviation from the area of a sphere with an equal mass. How this also influences the signal from any particular impact detection method (e.g., measurement of the acoustic signal or light flash generated during an impact) remains to be determined, and should not simply be assumed as well approximated by impacts from spheres.

One positive outcome of these results, is (partial) validation of the concept of using optical images of holes in thin films to determine impactor shape (adjusted for aspect during impact). This is important for mission proposals such as SAILOR/OPTIMIST, which plan to use such imaging of large (100+ μm) sized holes in thin Kapton films, as an aid in separating impacts by orbital debris from those by natural cosmic dust grains [29]. Such a separation is important when determining the sources of the total dust flux in Low Earth Orbit, in order to monitor the flux arising from just orbital debris. However, as discussed, it is not possible to associate a unique impactor shape with a given hole shape. Nevertheless, a separation into more spherical vs. non-spherical shaped objects, i.e., natural cosmic dust vs. debris, will still be possible in general.

Several areas remain for further investigation. For example, determining any dependence of the hole size on impact speed is important. As shown in Fig. 1, many impacts by debris will be at speeds above 10 km s^{-1} for example, so the ability to predict what happens at such speeds will be important. Also, in space, it is likely that any Kapton films used will be coated with thin metallic layers to help with thermal control. Whether or not these alter the hole shape or influence the presence of tears from an impact should be determined. The presence of tears is itself significant, as in Low Earth Orbit, any thin film like Kapton is susceptible to damage by atomic oxygen. Coatings help prevent this, but the exposure of the raw Kapton at hole edges and via tearing will increase the risk (e.g., see Ref. [68]).

In summary, whilst the importance of impacts by irregularly shaped debris is increasingly recognised for impact damage (such as penetration of bumpershield designs) and studied via laboratory testing and simulation (e.g., Refs. [46,47,69]), similar attention also has to be focussed on penetration of thin films. The results here apply in the thin film regime for impacts, and given the difficulties of deploying in space large area films of thickness less than say a few μm, this limits the current results to impactors typically larger than 100 μm. The influence of shape on holes from smaller, more frequent impactors in the size range say 10–100 μm, which fall into the transition regime of hole vs. projectile size (see Fig. 11), still has to be properly demonstrated, as has the fate of the impactor in such cases.

CRediT authorship contribution statement

M.J. Burchell: Writing – original draft, Methodology, Investigation, Formal analysis, Conceptualization. **L.A. Alesbrook:** Writing – review & editing, Resources, Methodology, Investigation. **M. van Ginneken:** Writing – review & editing, Resources, Methodology. **P.J. Wozniakiewicz:** Writing – review & editing, Resources, Methodology, Funding acquisition, Formal analysis.

Declaration of competing interest

The authors declare that they have no known competing financial interests or personal relationships that could have appeared to influence the work reported in this paper.

Acknowledgements

We thank the University of Kent for funding this work.

References

[1] J.-C. Liou, N.L. Johnson, Risks in space from orbiting debris, Science 311 (2006) 340–341, https://doi.org/10.1126/science.1121337.
[2] P.J. Wozniakiewicz, M.J. Burchell, Space dust and debris near the Earth, Astron. Geophys. 60 (2019) 38–42, https://doi.org/10.1093/astrogeo/atz150.
[3] ESA's Annual Space Environment Report. Technical Report, European Space Agency, Paris, France. Space_Environment_Report_latest.pdf (accessed 13 November. 2025). .
[4] C. Pardini, L. Anselmo, The short-term effects of the cosmos 1408 fragmentation on neighboring inhabited space stations and large constellations, Acta Astronaut. 210 (2023) 465–473, https://doi.org/10.1016/j.actaastro.2023.02.043.
[5] B.G. Cour Palais, Hypervelocity impact in metals, glass and composites, Int. J. Impact Eng. 5 (1987) 221–237, https://doi.org/10.1016/0734-743X(87)90040-6.
[6] D.J. Kessler, B.G. Cour-Palais, Collision frequency of artificial satellites: the creation of a debris belt, J. Geophys. Res. 83 (A6) (1978) 2637–2646.
[7] M. Bigdeli, R. Srivastava, M. Scaraggi, Mechanics of space debris removal: a review, Aerospace 12 (2025) 277, https://doi.org/10.3390/aerospace12040277.
[8] A. Eken, S. Eken, A parametrical study on hypervelocity impact of orbital debris, Aerospace 11 (10) (2024) 819, https://doi.org/10.3390/aerospace11100819.
[9] Space debris mitigation (ESA). https://technology.esa.int/page/space-debris-mitigation accessed 13 November. 2025).
[10] Orbital debris mitigation (NASA). https://orbitaldebris.jsc.nasa.gov/mitigation/.
[11] ORDEM 3.2, OD Engineering model (NASA). https://orbitaldebris.jsc.nasa.gov/modeling/ordem.html.
[12] Space debris user portal (ESA). https://sdup.esoc.esa.int/(accessed 13 November. 2025).
[13] D.J. Kessler, R.C. Reynolds, P.D. Anz-Meador, Orbital Debris Environment for Spacecraft Designed to Operate in Low Earth Orbit, National Aeronautics and Space Administration Johnson Space Center, Houston, Texas, 1989. NASA TM 100-471, https://apps.dtic.mil/sti/citations/ADA339021.
[14] F. Hörz, Cratering and penetration experiments in aluminum and teflon: implications for space-exposed surfaces, Meteoritics Planet Sci. 47 (2012) 763–797, https://doi.org/10.1111/j.1945-5100.2012.01354.x.
[15] D.J. Gardner, J.A.M. McDonnell, I. Collier, Hole growth characterisation for hypervelocity impacts in thin targets, Int. J. Impact Eng. 19 (7) (1997) 589–602, https://doi.org/10.1016/S0734-743X(96)00047-4.
[16] Y. Lu, J. Chen, D. Feng, et al., Numerical modeling of hypervelocity impacts on carbon fiber reinforced plastics using a GPU-accelerated SPH model, Comput. Mech. 72 (2023) 907–926, https://doi.org/10.1007/s00466-023-02318-7.
[17] M. Rival, J. Mandeville, Modeling of ejecta produced upon hypervelocity impacts, Space Debris 1 (1999) 45–57, https://doi.org/10.1023/A:1010021403591.
[18] M.J. Burchell, I.D.S. Grey, Oblique hypervelocity impacts on thick glass targets, Mater. Sci. Eng., A 303 (1–2) (2001) 134–141, https://doi.org/10.1016/S0921-5093(00)01847-5.
[19] W. Benz, E. Asphaug, Catastrophic disruptions revisited, Icarus 142 (1) (1999) 5–20, https://doi.org/10.1006/icar.1999.6204.
[20] N.L. Johnson, P.H. Krisko, J.-C. Liou, P.D. Anz-Meador, NASA's new breakup model of evolve 4.0, Adv. Space Res. 28 (9) (2001) 1377–1384, https://doi.org/10.1016/S0273-1177(01)00423-9.
[21] S.T. Stewart, Z.M. Leinhardt, Velocity-dependent catastrophic disruption criteria for planetesimals, ApJ 691 (2009) L133–L177, https://doi.org/10.1088/0004-637X/691/2/L133.
[22] D.E. Gault, J.A. Wedekind, The destruction of tektites by micrometeoroid impact, J. Geophys. Res. 74 (27) (1969) 6780–6794, https://doi.org/10.1029/JB074i027p06780.
[23] A.J.W. Morris, M.J. Burchell, Laboratory tests of catastrophic disruption of rotating bodies, Icarus 296 (2017) 91–98, https://doi.org/10.1016/j.icarus.2017.05.016.
[24] S. Marchi, D.D. Durda, C.A. Polanskey, E. Asphaug, W.F. Bottke, L.T. Elkins-Tanton, et al., Hypervelocity impact experiments in iron-nickel ingots and iron meteorites: implications for the NASA psyche mission, J. Geophysical Res. Planets 125 (2020), https://doi.org/10.1029/2019JE005927.
[25] J. Leliwa-Kopystyński, M.J. Burchell, D. Lowen, Impact cratering and break up of the small bodies of the solar system, Icarus 195 (2) (2008) 817–826, https://doi.org/10.1016/j.icarus.2008.02.010.
[26] K.H. Harriss, M.J. Burchell, Catastrophic disruption of hollow ice spheres. Planet, Sci. J. 1 (2020) 19, https://doi.org/10.3847/PSJ/ab8f34.
[27] R. Corsaro, F. Giovane, J.-C. Liou, M. Burchell, M. Cole, E. Williams, N. Lagakos, A. Sadilek, C. Anderson, Characterization of space dust using acoustic impact detection, J. Acoust. Soc. Am. 140 (2) (2016) 1429–1438, https://doi.org/10.1121/1.4960782.
[28] L.T. Cornwell, P.J. Wozniakiewicz, M.J. Burchell, L.A. Alesbrook, R.D. Corsaro, F. Giovane, J.-C. Liou, A study on the capabilities and accuracy of Kapton based TOF space dust and debris detector, Adv. Space Res. 72 (2023) 2959–2970, https://doi.org/10.1016/j.asr.2022.07.022.
[29] B.T. Varga, G. Mezohegyi, N. Keseru, D. Milankovich, G. Puttich, M.J. Burchell, P. J. Wozniakiewicz, A new large area detector for In-Situ observation of small anthropogenic debris in Low Earth Orbit – sailor, in: S. Lemmens, T. Flohrer, F. Schmitz (Eds.), Proc. 9th European Conference on Space Debris, published by the ESA Space Debris Office, Bonn, Germany, 2025, p. 8, 1–4 April 2025, https://conference.sdo.esoc.esa.int/proceedings/sdc9/paper/338/SDC9-paper338.pdf.
[30] P. Mancini, J. Williamsen, J. Heagy, B. Stellingwerf, Lethal debris creation following catastrophic and sub-catastrophic untracked orbital debris impacts on smallsats, in: Proceedings of the 2024 17th Hypervelocity Impact Symposium, ASME, Tsukuba, Japan, 2024 V001T01A001, https://doi.org/10.1115/HVIS2024-037. September 9–13, 2024.
[31] Heather Cowardin, Corbin Cruz, James Murray, et al., Updates on the DebriSat hypervelocity experiment and characterization of fragments in support of environmental models, Int. J. Impact Eng. 180 (2023) 104669, https://doi.org/10.1016/j.ijimpeng.2023.104669.
[32] P.H. Krisko, M. Horstman, M.L. Fudge, SOCIT4 collisional-breakup test data analysis: with shape and material characterization, Adv. Space Res. 41 (7) (2008) 1138–1146.
[33] K. Nakashima, T. Hanada, Y. Akahoshi, et al., Low-velocity catastrophic impact on micro satellite, in: Proceedings of the Fourth European Conference on Space

Debris, ESOC, Darmstadt, Germany, 18–20 April, 2005 (ESA SP-587, August 2005), ESA Publications Divisions, ESTEC, Noordwijk, The Netherlands, 2005, pp. 701–704, 2005. SP-587, Proceedings.
[34] T. Hanada, J.-C. Liou, Comparison of fragments created by low- and hyper-velocity impacts, Adv. Space Res. 41 (7) (2008) 1132–1137, https://doi.org/10.1016/j.asr.2007.05.062.
[35] T. Hanada, J.-C. Liou, T. Nakajima, E. Stansbery, Outcome of recent satellite impact experiments, Adv. Space Res. 44 (5) (2009) 558–567, https://doi.org/10.1016/j.asr.2009.04.016.
[36] H. Cowardin, et al., Updates to the DebriSat project in support of improving breakup models and orbital debris risk assessments, in: Proceedings of the 2019 Hypervelocity Impact Symposium, April 14-19, 2019, in: https://asmedigitalcollection.asme.org/hvis/proceedings/HVIS2019/883556/V001T10A012/1085253.
[37] H. Cowardin, et al., Updates on the DebriSat hypervelocity experiment and characterization of fragments in support of environmental models, in: Proceedings of the 2022 Hypervelocity Impact Symposium. Alexandria, VA, 2022. September 18–22, https://ntrs.nasa.gov/api/citations/20220009373/downloads/Cowardin_DebriSat%20Hypervelocity_Fragments_HVIS%202022_FINAL.pdf.
[38] S. Lan, S. Liu, Y. Li, F. Ke, J. Huang, Debris area distribution of spacecraft under hypervelocity impact, Acta Astronaut. 105 (1) (2014) 75–81, https://doi.org/10.1016/j.actaastro.2014.08.011.
[39] H. Abdulhamid, D. Bouat, A. Colle, J. Lafite, J. Limido, I. Midani, et al., On-ground HVI on a nanosatellite. Impact test, fragments recovery and characterization, impact simulations, 8th European Conference on Space Debris (2021), in: https://conference.sdo.esoc.esa.int/proceedings/sdc8/paper/140/SDC8-paper140.pdf.
[40] L. Olivieri, P.A. Smocovich, C. Giacomuzzo, A. Francesconi, Characterization of the fragments generated by a picosatellite impact experiment, Int. J. Impact Eng. 168 (2022) 104313, https://doi.org/10.1016/j.ijimpeng.2022.104313.
[41] R.H. Morrison, A Preliminary Investigation of Projectile Shape Effects in Hypervelocity Impact of A Double-Sheet Structure, 1972, p. 13. NASA Report No. TN-D-6944, https://ntrs.nasa.gov/api/citations/19720022272/downloads/19720022272.pdf.
[42] M.J. Burchell, N.G. Mackay, Crater ellipticity in hypervelocity impacts on metals, J. Geophys. Res. 103 (E10) (1998) 22761–22774, https://doi.org/10.1029/98JE02143.
[43] A.T. Kearsley, G.A. Graham, M.J. Burchell, M.J. Cole, P. Wozniakiewicz, N. Teslich, E. Bringa, F. Hörz, J. Blum, T. Poppe, Micro-craters in aluminum foils: implications for dust particles from comet Wild 2 on NASA's stardust spacecraft, Int. J. Impact Eng. 35 (12) (2008) 1616–1624, https://doi.org/10.1016/j.ijimpeng.2008.07.006.
[44] P.J. Wozniakiewicz, A.T. Kearsley, H.A. Ishii, M.J. Burchell, J.P. Bradley, N. Teslich, M.J. Cole, M.C. Price, The origin of crystalline residues in stardust Al foils: surviving cometary dust or crystallized impact melts? Meteoritics Planet Sci. 47 (2012) 660–670, https://doi.org/10.1111/j.1945-5100.2011.01328.x.
[45] R. Carriere, A. Cherniaev, Hypervelocity impacts on satellite sandwich structures—A review of experimental findings and predictive models, Appl. Mech. 2 (2021) 25–45, https://doi.org/10.3390/applmech2010003.
[46] H. Cowardin, E. Christiansen, M. Matney, et al., Orbital debris shape effect investigations for mitigating risk, J. Astronaut. Sci. 71 (2024) 49, https://doi.org/10.1007/s40295-024-00471-6.
[47] M. Schimmerohn, E. Watson, N. Durr, R. Putzar, B. Jilete, S. Lemmens, On the effect of impactor shape on CFRP spacecraft structures, in: S. Lemmens, T. Flohrer, F. Schmitz (Eds.), Proc. 9th European Conference on Space Debris, published by the ESA Space Debris Office, Bonn, Germany, 2025, p. 10, 1–4 April 2025, https://conference.sdo.esoc.esa.int/proceedings/sdc9/paper/303/SDC9-paper303.pdf.
[48] K.-P. Bouzoukis, G. Moraits, V. Kostopoulos, V. Lappas, An overview of CubeSat missions and applications, Aerospace 12 (2025) 550, https://doi.org/10.3390/aerospace12060550.
[49] T. Villela, C.A. Costa, A.M. Brandão, F.T. Bueno, R. Leonardi, Towards the thousandth CubeSat: a statistical overview, International Journal of Aerospace Engineering 2019 (2019) 5063145, https://doi.org/10.1155/2019/5063145.
[50] L.T. Cornwell, M.J. Burchell, P.J. Wozniakiewicz, Feasibility of using CubeSats and small detectors for in-situ space debris and cosmic dust flux measurement, Adv. Space Res. 75 (9) (2025) 6944–6959, https://doi.org/10.1016/j.asr.2024.06.058.
[51] A.T. Kearsley, R.P. Webb, G.W. Grime, P.J. Wozniakiewicz, M.C. Price, M. J. Burchell, T. Salge, J. Spratt, Cosmic dust impacts on the Hubble Space Telescope, Phil. Trans. R. Soc. A 382 (2024) 20230194, https://doi.org/10.1098/rsta.2023.0194.
[52] J. Hamilton, J.-C. Liou, P. Anz-Meador, B. Corsaro, F. Giovane, M. Matney, E. Christiansen, Development of the space debris sensor, in: T. Schmitz, F. Flohrer (Eds.), Proceedings of the 7th European Conference on Space Debris. Pub, ESA Space Debris Office, 2017, p. 11, in: https://conference.sdo.esoc.esa.int/proceedings/sdc7/paper/965.
[53] P. Anz-Meador, M. Ward, A. Manis, K. Nornoo, B. Dolan, C. Claunch, J. Rivera, The space debris sensor experiment, in: First Int'L Orbital Debris Conf, The Space Debris Sensor Experiment - NASA Technical Reports Server (NTRS), 2019, pp. 1–10.
[54] L.S. Alesbrook, M.J. Burchell, L.T. Cornwell, R.D. Corsaro, F. Giovane, J.-C. Liou, J. Tandy, P.J. Wozniakiewicz, Hypervelocity impact induced light flash experiments on single and dual layer kapton targets to develop a time of flight space dust and debris detector, Int. J. Impact Engng. 187 (2024) 104897, https://doi.org/10.1016/j.ijimpeng.2024.104897.
[55] N. Ledford, M. Schimmerohn, C. Horch, R. Putzar, S. Busch, M. Millinger, In-situ detection of small space debris with the LArID concept: breadboard verification and the path to a flight mission, in: S. Lemmens, T. Flohrer, F. Schmitz (Eds.), Proc. 9th European Conference on Space Debris, Bonn, Germany, 1–4 April 2025, Published by the ESA Space Debris Office, 2025, p. 7. SDC9-paper262.pdf.
[56] Y. Tsuda, O. Mori, R. Funase, H. Sawada, T. Yamamoto, T. Saiki, T. Endo, J. Kawaguchi, Flight status of IKAROS deep space solar sail demonstrator, Acta Astronaut. 69 (9–10) (2011) 833–840, https://doi.org/10.1016/j.actaastro.2011.06.005.
[57] W.K. Wilkie, The NASA advanced composite solar sail system (ACS3) flight demonstration: a technology pathfinder for practical smallsat solar sailing, in: 35th Annual Small Satellite Conference, Logan, Utah, USA, 2021, pp. 1–15, 2021, https://digitalcommons.usu.edu/cgi/viewcontent.cgi?article=5020&context=smallsat.
[58] M.J. Burchell, M.J. Cole, J.A.M. McDonnell, J.C. Zarnecki, Hypervelocity Impact Studies Using the 2 MV Van de Graaff Dust Accelerator and Two Stage Light Gas Gun of the University of Kent at Canterbury, Meas, Sci. Tech. 10 (1999) 41–50. https://iopscience.iop.org/article/10.1088/0957-0233/10/1/011/pdf.
[59] S.G. Love, D.E. Brownlee, N.L. King, F. Hörz, Morphology of meteoroid and debris impact craters formed in soft metal targets on the LDEF satellite, Int. J. Impact Eng. 16 (3) (1995) 405–418, https://doi.org/10.1016/0734-743X(94)00050-7.
[60] N. Pailer, E. Grün, The penetration limit of thin films, Planet. Space Sci. 28 (3) (1980) 321–331, https://doi.org/10.1016/0032-0633(80)90021-5.
[61] M.J. Neish, S.P. Deshpande, S. Kibe, H. Yano, Y. Kitazawa, S. Yamamoto, Micrometeoroid and space debris impacts on the space flyer unit, and hypervelocity impact calibration of its surfaces, in: Second European Conference on Space Debris, ESA Publication SP-393, ESOC, Darmstadt, Germany, 1997, pp. 177–182, 17-19 March 1997.
[62] M. Neish, S. Kibe, Hypervelocity impact damage equations for Kapton multilayered insulation and teflon second-surface mirrors, in: Proceedings of the 3rd European Conference on Space Debris, ESOC, Darmstadt, Germany, 2001, 19 - 21 March 2001 (ESA SP-473, August 2001), https://conference.sdo.esoc.esa.int/proceedings/sdc3/paper/48/SDC3-paper48.pdf.
[63] N.N. Smirnov, V.F. Nikitin, L.I. Stamov, V.V. Tyurenkova, M.N. Smirnova, Modelling of thin wall perforation limit in debris particles impact on space structures, Acta Astronaut. 204 (2023) 831–839, https://doi.org/10.1016/j.actaastro.2022.09.026.
[64] Dupont Kapton summary of properties data sheet. https://www.beta.dupont.com/content/dam/electronics/amer/us/en/electronics/public/documents/en/EI-10142_Kapton-Summary-of-Properties.pdf, 2022 (accessed 2 January, 2026).
[65] D.J. Weidman, Simplified ballistic-limit expressions for thin sheets. Simplified ballistic-limit Expressions for Thin Sheets, 1969, p. 17. NASA TN-5559.
[66] R. Verker, N. Eliaz, I. Gouzman, S. Eliezer, M. Fraenkel, S. Maman, F. Beckmann, K. Pranzas, E. Grossman, The effect of simulated hypervelocity space debris on polymers, Acta Mater. 52 (19) (2004) 5539–5549, https://doi.org/10.1016/j.actamat.2004.08.013.
[67] Tao Liu, Zhixin Zeng, Xinghua Zhang, Xinming Qiu, ZhengAi Cheng, Li Wang, Shaoxia Jia, Jian Cai, Performance of polyimide film under hypervelocity impact of micro flyer: experiments and simulations, Acta Astronaut. 159 (2019) 452–470, https://doi.org/10.1016/j.actaastro.2019.01.038.
[68] A. Dignam, P. Wozniakiewicz, M. Burchell, L.S. Alesbrook, A. Tighe, A. Suliga, J. Wessing, A. Kearsley, J. Bridges, J. Holt, S. Howie, L. Peatman, D. Fitzpatrick, Palladium-coated Kapton for use on dust detectors in Low Earth Orbit: performance under hypervelocity impact and atomic oxygen exposure, Front. Space Technol. 3 (2022) 933664, https://doi.org/10.3389/frspt.2022.933664.
[69] P. Domingo, I. Telichev, Correlating the impact severity of spherical and non-spherical projectiles at hypervelocity, Aerospace 12 (2025) 941, https://doi.org/10.3390/aerospace12100941.



MARK J. BURCHELL received a BSc (1st class) in physics from the University of Birmingham (UK), a PhD (physics) from Imperial College London, was a post-doctoral researcher at Imperial College and the University of California (Santa Cruz), and a Fellow at CERN. He then became a faculty member in space science at the University of Kent (UK), where he is now Emeritus Professor. He specialises in experimental studies of hypervelocity impacts relating to the Solar System and spacecraft.



LUKE A. ALESBROOK received a MPhys in astronomy, space science and astrophysics from the University of Kent. He then took a PhD at Kent specialising in entry of cosmic dust into the atmosphere. He has run the impact facility at Kent since 2020.



MATTHIAS VAN GINNEKEN has a Masters in Planetology from Univ. Paris XI (Orsay) and a PhD from Università degli Studi di Siena, Italy (specialising in studies of micrometeorites). He held postdoctoral positions at the Korea Polar Research Institute, (Rep. of Korea), Imperial College London, and the Université Libre de Bruxelles, (Belgium), again specialising in micrometeorites. He moved to the University of Kent in 2019 to work on cosmic dust.



PENELOPE J WOZNIAKIEWICZ holds a MSci in planetary sciences from University College London and a PhD in planetary science from Imperial College London. She was a postdoctoral researcher at the Institute of Geophysics & Planetary Physics (Lawrence Livermore National Laboratory, California) and at the University of Kent. She was then a Marie Curie International Fellow at the Natural History Museum (London). Since 2015 she has been a faculty member in Space Science at the University of Kent. She specialises in cosmic dust and space debris, as well as in cometary science and developing techniques to capture dust in space.